

## Article

# Precipitable Water Content Climatology over Poland

Hanna Ojrzyńska \* , Marek Błaś  and Maciej Kryza 

Faculty of Earth Science and Environmental Management, University of Wrocław, 50-137 Wrocław, Poland; marek.blas@uwr.edu.pl (M.B.); maciej.kryza@uwr.edu.pl (M.K.)

\* Correspondence: hanna.ojrzyńska@uwr.edu.pl

**Abstract:** In this work, the high-resolution spatial and temporal variability of precipitable water (PW) over Poland is presented. PW is one of the key parameters of the atmosphere taken into account in thermodynamic and radiation models. The daily PW values from years 2001–2010, calculated with the use of the WRF model, were compared with PW from soundings. The WRF modeled PW is in close agreement with measurements for the whole column of the troposphere and for individual levels: below 1.5 km, 1.5–3 km, 3–6 km and 6–10 km. The best agreement is observed in the lower part of the troposphere, especially for winter months. At the levels of 1.5 km to 10 km, the WRF model overestimates the PW values throughout the year, whereas up to 1.5 km PW is underestimated. The study shows an increasing trend of PW annual values between 1983 and 2010, but the trend is statistically insignificant. A significant positive trend with a high Sen's slope is observed for the summer season up to 3 km in the troposphere, along with a significant negative tendency for spring. The trends in PW over Poland and Central Europe identified in this study contribute to the ongoing discussion on the observed climate changes.

**Keywords:** precipitable water; the Weather Research and Forecasting model; atmospheric soundings; spatial variability; Poland



**Citation:** Ojrzyńska, H.; Błaś, M.; Kryza, M. Precipitable Water Content Climatology over Poland. *Atmosphere* **2022**, *13*, 988. <https://doi.org/10.3390/atmos13060988>

Academic Editor: Eduardo García-Ortega

Received: 15 May 2022

Accepted: 17 June 2022

Published: 19 June 2022

**Publisher's Note:** MDPI stays neutral with regard to jurisdictional claims in published maps and institutional affiliations.



**Copyright:** © 2022 by the authors. Licensee MDPI, Basel, Switzerland. This article is an open access article distributed under the terms and conditions of the Creative Commons Attribution (CC BY) license (<https://creativecommons.org/licenses/by/4.0/>).

## 1. Introduction

Precipitable water vapor content (PW), also called integrated water vapor or integrated precipitable water vapor, is an important parameter in the study of atmospheric processes. According to the definition of the Glossary of Meteorology AMS [1], precipitable water is the total atmospheric water vapor contained in a vertical column of air, expressed in terms of the height to which that water substance would stand if completely condensed. PW is commonly expressed in mm or  $\text{kg}\cdot\text{m}^{-2}$ . Bordi et al. [2] state that PW represents the maximum potential precipitation and the supply of latent heat available to develop and maintain storm processes. They underline, similarly as Tuller did earlier [3], that the quantity of precipitation noted at meteorological stations is correlated with PW values, but also with the initial degree of saturation of water vapor and the dynamic mechanisms that provide the cooling necessary to produce saturation and trigger the droplets' growth. For this reason, the correlation between precipitation amounts and precipitable water vapor of air masses is not clear [2,4] and changes over seasons [5] or with land cover [6].

Precipitable water in the atmosphere influences not only the water balance by participating in cloud formation and precipitation, but it also plays an important role in shaping the heat balance in the atmosphere, modulating radiation by processes of absorption, scattering and reflection [7–11]. The newest results of analysis of atmospheric water vapor radiative effects on shortwave solar radiation under clear skies [10] show that the reduction of solar radiation reaches globally  $-80.2 \text{ W m}^{-2}$  with a remarkable seasonal and spatial pattern. From this point of view, the PW is an important element in solar forecasting and historical solar database production. On the other hand, water vapor is an important greenhouse gas that strongly absorbs the infrared and longwave range radiation [12–15]. Finally, the water in the atmosphere is the energy carrier, releasing or accumulating its

resources during phase transitions, so it is a significant link in the energy exchange between atmosphere and ocean. Therefore, the water content in the atmosphere is taken into account in global and regional meteorological models [16–18]. In practice, PW is used to increase the accuracy of weather forecasts [19–26] and explains the course and occurrence of extreme weather events, such as heavy precipitation, violent storms, super-cell thunderstorms and others [27–33]. Analyzing PW trends is also crucial because of the observed climate change [16,18,32,34].

At a global scale, the main process controlling moisture content in the atmosphere is evaporation over the oceans in tropical zones and atmospheric circulation [35]. Precipitable water is used to identify atmospheric rivers—that is, long, narrow and transient corridors of strong horizontal water vapor being transported to a higher latitude, which are typically associated with a low-level jet stream ahead of the cold front of an extratropical cyclone [36–38]. Atmospheric rivers can lead to heavy precipitation whenever these systems are forced upward, either by mountains or by ascent in the warm conveyor belt. The other is the integrated water vapor transport (IVT), which is dependent on both the amount of moisture and the strength of the flow, and calculating it requires profiles of both moisture and wind. The importance of IVT in extreme precipitation events and floods has been analyzed in detail for the west coast of the USA [36,39,40]. Similar conclusions have also been reached for Europe [41–44].

The number of methods for observation of PW has increased considerably during the last decades and now includes optical ground-based and satellite soundings. These modern techniques enable us to follow the quick changes in column water vapor content. The use of a sounding balloon is the traditional method that allows for an accurate determination of precipitable water data [45–47]. Satellite methods using Atmospheric Infrared Sounders [5,48,49] or methods based on slant observations of tropospheric delay of Global Navigation Satellite System (GNSS) [50–53] are also commonly used. However, the limitations of radiosonde data, as well as other observation techniques, for climate research is that the derived PW is not homogeneous over long time periods due to calibration uncertainties and sensor changes [54]. Due to its high cost [55], the density of the radiosonde measuring stations and the frequency of measurements vary in space and are usually low (e.g., three stations in Poland, each with two soundings per day). Data of PW derived from GNSS observations may be affected by changes in the electromagnetic environment around the antenna [54]. Advanced GNSS processing techniques also require external precise satellite clock corrections consistent with orbits as well as precise models for undifferenced observations required for precise point positioning [56]. For this reason, in recent years the data from mesoscale atmospheric models have become a complementary alternative to the measurements. With the development of global and mesoscale meteorological models (e.g., GFS, GEM, KNMI-HIRLAM, ARPÈGE, ICON, HRES and ENS) and dynamical downscaling techniques, the gridded data from these models have provided characteristics of the spatial and temporal distribution of PW over large areas. This information is often available at high spatial and temporal resolution [2,35,57]. Numerical weather prediction models such as WRF have been tested in various regions, and they have turned out to be very effective in the simulation of PW profiles [31,58].

Multi-year values of precipitable water content were used by Wypych et al. [35] to identify and characterize humidity regions in Europe. According to this classification, the area of Poland belongs to the mid-continental region, characterized by the largest moisture content in the summer and moisture deficit in the winter, which complies with an earlier characteristic of PW in Poland by Kożuchowski [59]. Wypych et al. [35] underline that the moisture content at lower levels (850 and 950 hPa) largely depends on the properties of the boundary layer (evaporation, temperature and its vertical structure), whereas in the upper troposphere (500 hPa), it reflects the influence of atmospheric circulation on the continental scale. Degirmendžić and Kożuchowski [60] showed that the extreme values of PW in Poland in the years 1958–2008 ranged from 1.9 mm to 41.0 mm, with an average of 15.9 mm. Maximum rainfall volume events in Poland occur under relatively high PW, but

the height of these maxima are poorly correlated with PW. Thus, the amount of maximum precipitation is primarily determined by the efficiency of precipitation processes [2]. The maximum daily rainfall occurred at PW exceeding 30 mm [59].

Aside from the aforementioned very few reports, the studies of PW variability and its trend over Central Europe and Poland are rare. This is due to the limited number of in situ stations with traditionally long periods of data records for meaningful exploration of PW, unlike other regions in the mid-latitude of the Northern Hemisphere. Preliminary results of the spatial variability of PW over Poland on the basis of GNSS data were presented in 2021 [61], supported with a geostatistical modeling approach for spatial interpolation. In our work, we have used high temporal and spatial resolution meteorological data, provided by the WRF model, to present the long-term gridded climatology of PW over Poland. First, we compare the modeled PW with measurements. Second, we analyze the trends in PW and their seasonal changes. The analysis is conducted not only in relation to the whole analyzed column of the troposphere (up to 5000 Pa), but also for individual levels at which the characteristic atmospheric processes take place. According to the authors' knowledge, this approach to PW data verification has not been previously presented in the literature.

## 2. Materials and Methods

The PW for this study was calculated for the period 1983–2010 with the use of the meteorological data from the Weather Research and Forecasting model (WRF) version 3.4.1 [62]. The model was run in reanalysis mode using three one-way nested domains covering Europe (45 km × 45 km grid), Central Europe (15 km × 15 km) and Poland (5 km × 5 km). All domains have 51 vertical layers. The temporal resolution was 3 h. ERA-Interim reanalysis was used as boundary and initial conditions [63]. The model configuration was selected after the running and evaluation of the model for the chosen test periods [64–66]. All domains use the same options of physics as summarized in Table 1, but for the innermost domain, convection is explicitly resolved [65]. The climatological analysis of PW concerns all grid cells covering the area of Poland, with the spatial resolution of 5 km × 5 km. The measurements for model evaluation are available from six stations of atmospheric soundings: Łeba, Legionowo, Lindenberg, Praha, Prostějov and Wrocław (Table 2). The soundings are performed at 00 UTC and 12 UTC.

**Table 1.** The WRF model physics options used in this study.

	d01	d02	d03
Short-wave radiation	RRTMG [67]		
Long-wave radiation	RRTM [68]		
Planetary boundary layer	Yonsei University scheme [69]		
Cumulus convection	Kain-Fritsch [70]		Explicitly resolved
Microphysics	Goddard [71]		
Land surface model	Noah land surface model		

**Table 2.** Atmospheric sounding stations.

Nr	Station	Code	$\phi$ (N)	$\lambda$ (E)	Elevation [m a.s.l.]
1.	Legionowo	12374	52.40	20.96	96
2.	Lindenberg	10393	52.21	14.11	115
3.	Łeba	12120	54.75	17.53	6
4.	Praha	11520	50.01	14.45	304
5.	Prostějov	11747	49.45	17.11	216
6.	Wrocław	12425	51.78	16.88	122

Due to the limited quality of data from all radiosonde stations, the evaluation period was performed for the years 2001–2010. For this period, all measuring stations used radiosonde instruments produced by the Finnish company Vaisala—RS-92. The RS-92 sensors were calibrated in the CAL-4 calibration machine, which is the world’s most advanced calibration machine for the mass production of sounding sensors [72]. The uncertainties for radiosonde are  $\pm 0.5$  °C,  $\pm 5\%$  and  $\pm 1$  hPa for temperature, relative humidity and atmospheric pressure, respectively [23,73]. All of the sounding stations have calibration certificates, which are regularly renewed (every 2 years). The use of the same sounding sensors at all stations throughout the entire analysis period (2001–2010) and the same calibration techniques allowed for homogeneity of the entire measurement series.

The calculation of PW based on meteorological data from the WRF model was performed at postprocessing stage, with the use of two tools implemented in NCAR Command Languages [74]. The first function, *wrf\_user\_getvar*—with indicated variable *pw*—extracts essential data from WRF outputs to calculate PW from the whole analyzed column of the troposphere. The second function, *prcwater\_dp*, additionally allows for limiting the levels from which the specific values of humidity (kg/kg) and pressure layer thickness (Pa) are taken to PW calculations. For this reason, the function was used to sum up the precipitable water content ( $\text{kg}\cdot\text{m}^{-2}$ ) for individual levels above the ground: up to 1.5 km, 1.5–3.0 km, 3.0–6.0 km, 6.0–10.0 km and over 10.0 km. In mountainous areas, some peaks exceed the height of the lowest layer (up to 1.5 km), and these grid cells were excluded from the analysis.

The data for model evaluation were prepared using atmospheric sounding profiles provided by the national weather services and available through the repository of the University of Wyoming (<http://weather.uwyo.edu/upperair/sounding.html>, accessed on 1 January 2021). Radiosondes typically measure temperature  $t$  (°C), relative humidity RH (%), and, in many cases, air pressure  $p$  (hPa). For the purposes of PW calculations, comparable to those of the model, the formula by Pérez-Jordán et al. [23] was applied, with the assumption of hydrostatic balance:

$$PW = \frac{10^5}{\rho g} \int_{p_t}^{p_s} r dp \quad (\text{mm}), \quad (1)$$

where  $g$  is the Earth’s gravity ( $\text{m}\cdot\text{s}^{-2}$ ),  $p_s$  and  $p_t$  are the pressure levels at the surface and top of the atmospheric column in hPa,  $r$  is the mixing ratio and  $dp$  is the difference in pressure between the assumed levels. To calculate the PW for individual heights, the  $p_s$  and  $p_t$  values were taken from the measurement heights closest to the assumed levels. The ideal gas law and Dalton’s law of partial pressures was applied to the formula of the mixing ratio, resulting in

$$r = 0.622 \left( \frac{e}{p - e} \right) \quad (2)$$

where the coefficient 0.622 is the ratio of molar masses of water vapor and dry air, and  $e$  is the partial vapor pressure that was obtained from the definition of relative humidity as

$$e = e_{sat} \frac{RH}{100} \quad (\text{hPa}), \quad (3)$$

where  $e_{sat}$  (hPa) is the saturation vapor pressure.

The procedure described above was used to calculate the PW for an air column covering the entire measured troposphere, but also for individual levels above the ground: up to 1.5 km, 1.5–3.0 km, 3.0–6.0 km, 6.0–10.0 km and over 10.0 km.

The WRF modeled PW was compared with PW calculated using radiosonde data. The model–measurement agreement was summarized using the Pearson correlation coefficient (with confidence level = 0.95) and root mean square error (RMSE). The statistics were calculated separately for individual levels, months and seasons. Because of the need to normalize the values, the RMSE was analyzed in comparison to the monthly and seasonal

averages and standard deviations of PW values.  $RMSE_{avg}$  was calculated as the percentage share of the RMSE value in the average PW value. For spring, the data from March to May were analyzed, for summer—from June to August, for autumn—from September to November and for winter—from December to February. All calculations were performed using R statistical software [75].

All maps of PW and the calculations of seasonal and monthly means (AVG), standard deviation (SD) or variability coefficients (VC—percentage value of standard deviation ratio to the average value) of PW values calculated from the WRF data for selected grids and for the area of Poland were prepared with the use of a standard postprocessing function in NCAR Command Language. Using the statistical function *trend\_manken*, the Mann–Kendall test for monotonic trends of PW times series were carried out and Sen’s slope estimators were calculated. The trend analysis was performed based on the annual and seasonal PW means and annual maximum values.

### 3. Results

#### 3.1. Model Evaluation

WRF modeled PW is compared with radiosonde data in Table 3 and Figure 1. The Pearson correlation coefficient reaches 0.97 for the whole analyzed period 2001–2010, with RMSE of 2.1 mm, which constitutes 13.6% of the average value of PW from sounding and about a quarter of the PW standard deviation accordingly. The smaller correlation coefficient is noted in summer months (0.92), with RMSE reaching 12.8% of the average value of PW, and the highest in autumn and winter (0.97 with  $RMSE_{avg}$  of 10.96% and 12.6% accordingly). Annual courses of PW standard deviation from sounding and from WRF model are very similar (Figure 2). However, the WRF model overestimates the values of PW throughout the year. The highest overestimation, reaching almost 2 mm in monthly means is observed in summer and spring months (Figure 2). Observed dependencies are characteristic for all analyzed stations with small differences between them (Figure 1).

**Table 3.** Pearson correlation coefficients ( $R^2$ ) and root mean square error in mm (RMSE) and % of PW average value ( $RMSE_{avg}$ ) between PW data from WRF model and soundings. AVG—values of averages; SD—standard deviation of PW from soundings; N—number of observations.

	$R^2$ (–)	RMSE (mm)	$RMSE_{avg}$ (%)	AVG (mm)	SD (mm)	N
<b>Years 2001–2010</b>	0.97	2.10	13.62	15.42	8.06	38,689
Spring	0.96	1.96	15.14	12.95	5.86	9800
Summer	0.92	3.08	12.80	24.07	6.84	9586
Autumn	0.97	1.74	10.96	15.88	6.25	9653
Winter	0.97	1.12	12.60	8.89	4.08	9650

Evaluation of PW for individual tropospheric levels shows differences between values from the model and from the soundings (Figures 3 and 4). The highest Pearson correlation coefficient, reaching 0.91, is observed for the level up to 1.5 km and between 3.0 and 6.0 km (Table 4).  $RMSE_{avg}$  for these levels does not exceed 23% and 44% of the average values of PW accordingly. At the levels of 1.5 to 3.0 km,  $RMSE_{avg}$  ranges between 40 and 50%, and from 6.0 km to 10 km exceeds 65%. The Pearson correlation coefficient in summer months is the lowest for all analyzed tropospheric levels, especially in the lower parts (up to 3.0 km), for which the  $R^2$  does not exceed 0.70 (Table 4).

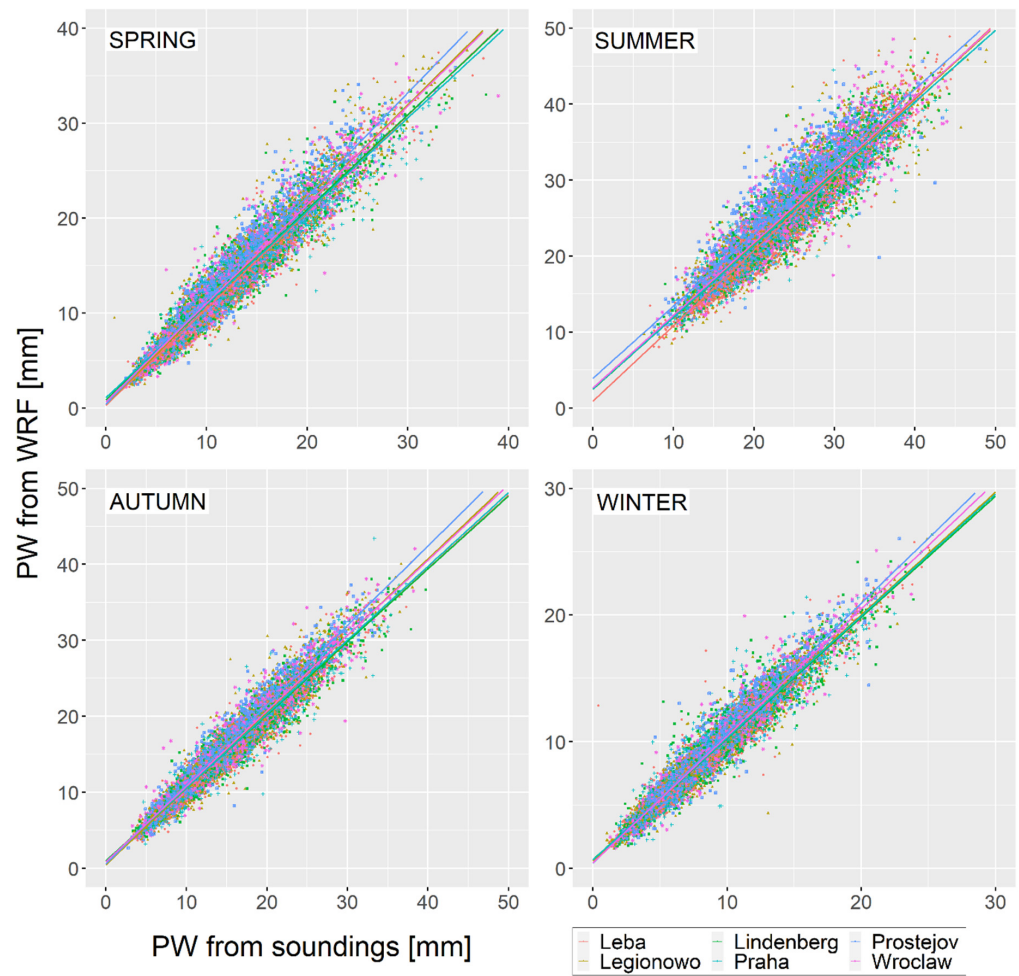


**Figure 1.** Comparison of PW data from the WRF model and data from atmospheric soundings between 2001 and 2010 in seasons.

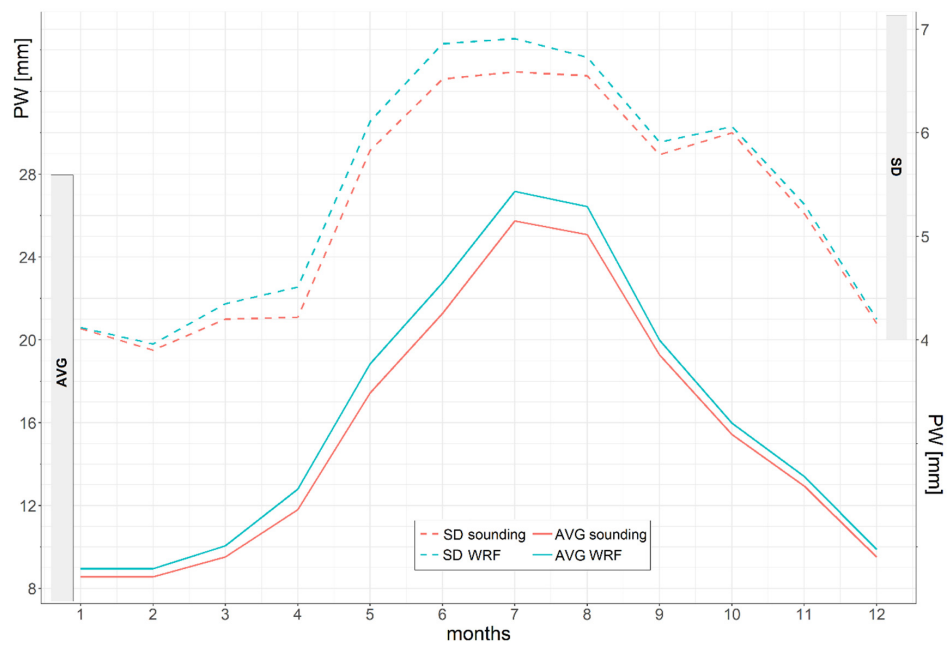


**Figure 2.** Monthly means (AVG) and standard deviation (SD) of PW (mm) from the WRF model and from soundings for the whole column of the troposphere in the years 2001–2010.

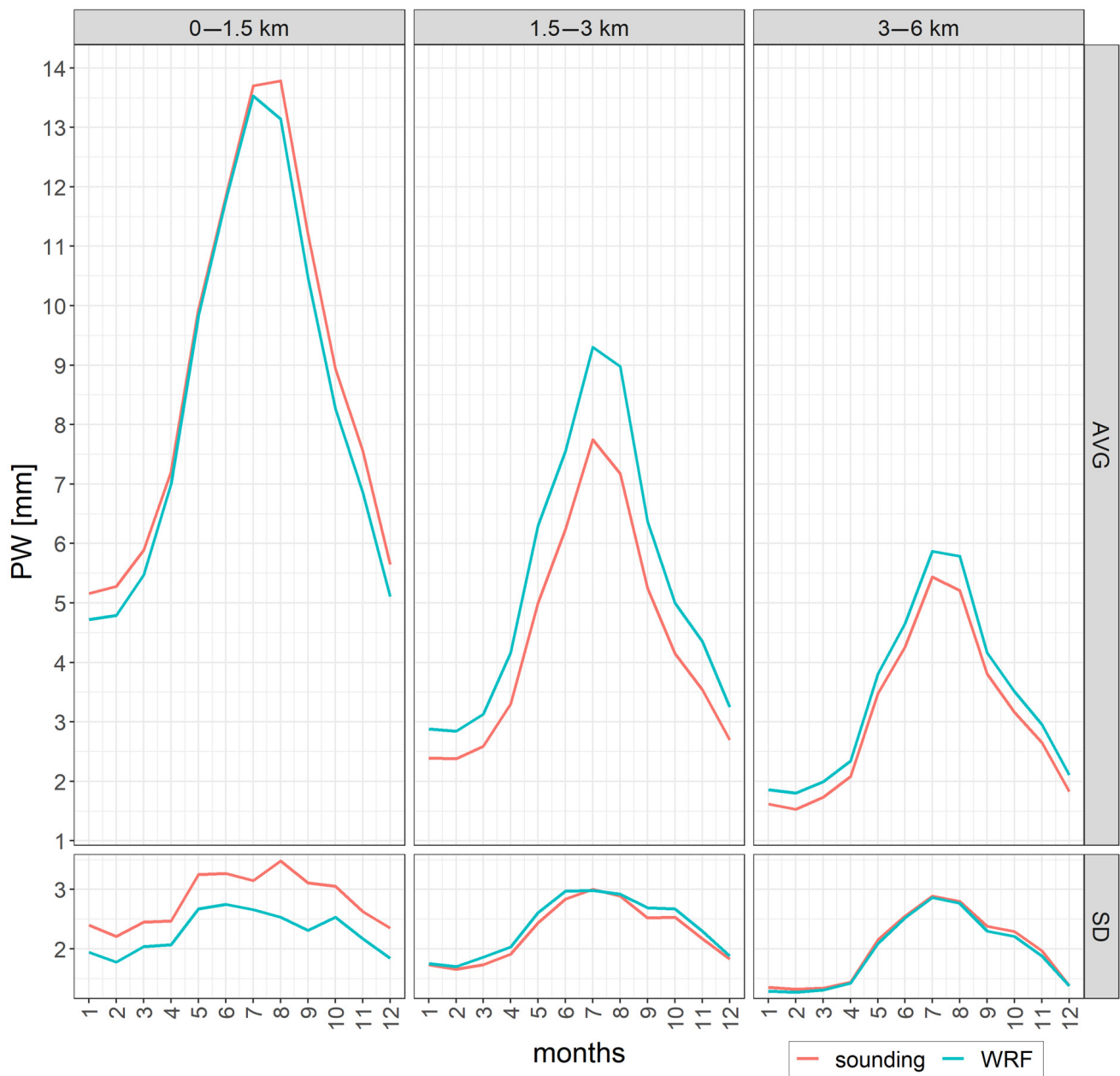


**Figure 3.** Monthly mean (AVG) and standard deviation (SD) of PW (mm) from the WRF model and soundings for individual levels of the troposphere in the years 2001–2010.

At the levels of 1.5 km to 10 km, the WRF model overestimates the PW values throughout the year, whereas up to 1.5 km it mainly underestimates them (Figures 3 and 4). For April to July at the level up to 1.5 km, the differences between modeled and observed PW are the smallest. For the remaining months, the WRF model underestimates PW values (up to 0.5 mm in monthly means). For the upper tropospheric levels, the overestimation of PW values by the WRF model is mostly visible at the highest level from 6 to 10 km. At these heights, the differences between WRF and sounding monthly means constitute 38% to 50% of the observed monthly means of PW. The differences in monthly means at the levels of 1.5 km to 6 km are lower and vary between 8% and 26% of the observed monthly values. At the level up to 1.5 km, the differences in PW means do not exceed 10% of the real PW means.

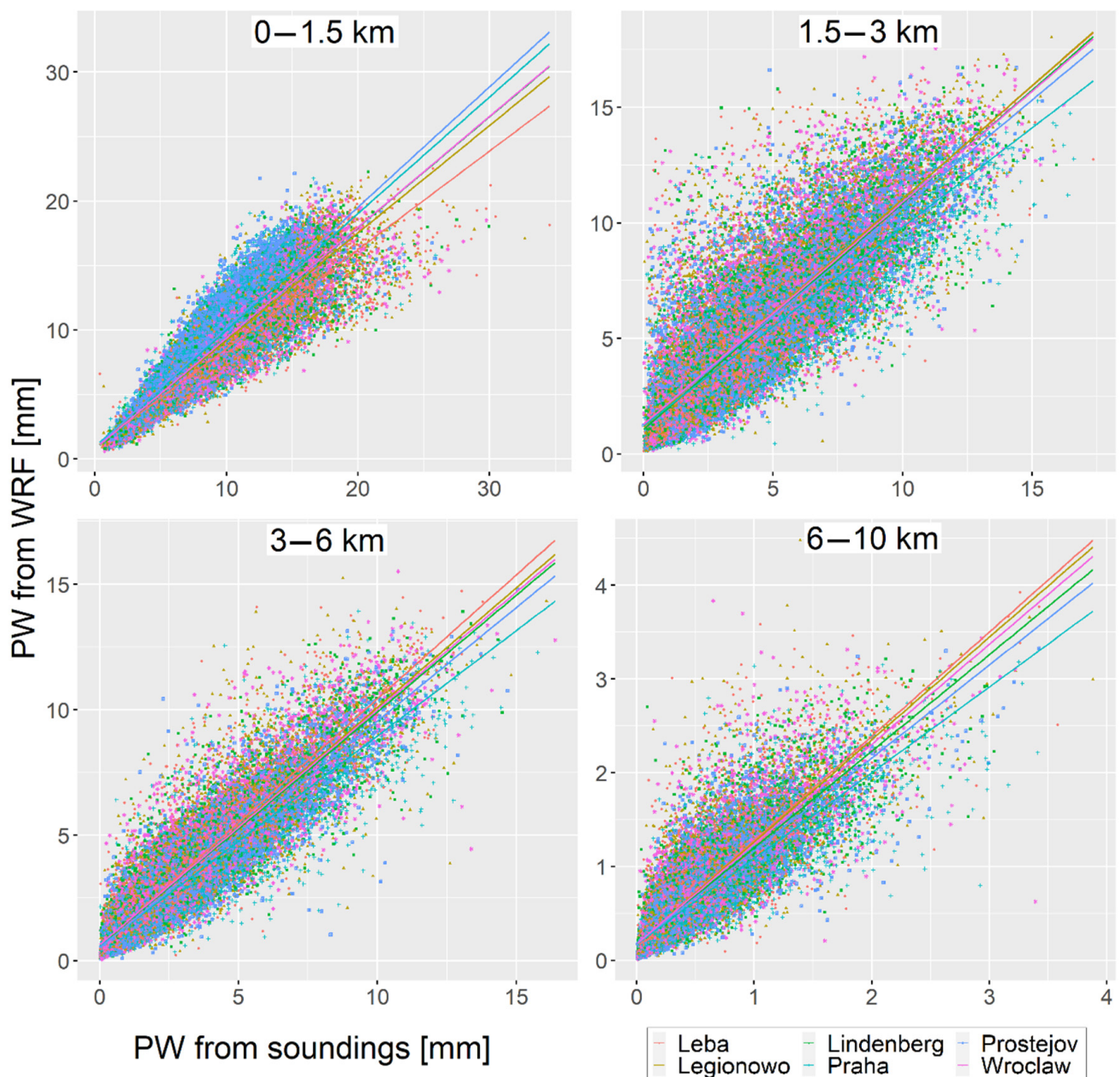


**Figure 4.** Comparison of PW data from WRF model and data from atmospheric soundings between 2001 and 2010 at individual levels: below 1.5 km, 1.5–3 km, 3–6 km and 6–10 km.

The annual courses of PW standard deviation from soundings and from the WRF model are very close at the tropospheric levels from 1.5 km to 6 km (Figure 3). At the level up to 1.5 km, the standard deviation from the WRF data is a smaller than from soundings, whereas at the highest part of troposphere above 6 km, it is larger. The values of SD from the WRF model at the level of 6 to 10 km for winter months are almost the same as the monthly means of PW from soundings (Table 4).

**Table 4.** Pearson correlation coefficients ( $R^2$ ) and root mean square error in mm (RMSE) and % of PW average value (RMSE<sub>avg</sub>) between PW data from the WRF model and soundings for individual troposphere levels. AVG—values of averages and SD—standard deviation of PW from soundings.

		2001–2010	Spring	Summer	Autumn	Winter
up to 1.5 km	$R^2$	0.91	0.87	0.70	0.87	0.89
	RMSE (mm)	1.83	1.64	2.48	1.79	1.20
	RMSE <sub>avg</sub> (%)	20.70	21.33	18.89	19.39	22.35
	AVG (mm)	8.84	7.69	13.13	9.23	5.37
	SD (mm)	4.19	3.23	3.42	3.30	2.33
1.5–3.0 km	$R^2$	0.84	0.80	0.70	0.79	0.81
	RMSE (mm)	2.02	1.81	2.82	1.92	1.19
	RMSE <sub>avg</sub> (%)	46.22	49.73	39.89	44.55	47.79
	AVG (mm)	4.37	3.64	7.07	4.31	2.49
	SD (mm)	2.95	2.29	2.98	2.52	1.75
3.0–6.0 km	$R^2$	0.91	0.89	0.87	0.90	0.88
	RMSE (mm)	1.08	0.91	1.51	1.04	0.72
	RMSE <sub>avg</sub> (%)	35.18	37.30	30.32	32.40	43.37
	AVG (mm)	3.07	2.44	4.98	3.21	1.66
	SD (mm)	2.46	1.85	2.80	2.27	1.36
6.0–10.0 km	$R^2$	0.86	0.84	0.80	0.85	0.84
	RMSE (mm)	0.33	0.23	0.51	0.32	0.16
	RMSE <sub>avg</sub> (%)	73.33	74.19	65.38	65.31	76.19
	AVG (mm)	0.45	0.31	0.78	0.49	0.21
	SD (mm)	0.44	0.28	0.55	0.41	0.20

### 3.2. Spatial Distribution of PW over Poland

The annual areal mean of PW over Poland in the years 1983–2010, calculated with the WRF model, reaches 15.8 mm (Table 5). The spatial variability of PW's annual value over Poland in the years 1983–2010 shows that PW decreases with height in mountainous region and falls to c.a. 8 mm in the highest part of the Sudetes and the Carpathian Mountains (Figure 5). Lower values of PW are noted also in the northern region of Poland, especially on the highest moraine hills and in the uplands in the south. Areal standard deviation of PW in the analyzed period reaches 8.3 mm and decreases to about 5 mm in the mountains and to 7 mm on the Baltic Sea coast (Figure 6). The areal variability coefficient (VC) reaches 52.7%. After excluding the mountainous area with the highest values of VC exceeding 60%, the variability coefficient over the area of Poland has a characteristically increasing tendency from the west to the east, fluctuating from 48 to 56% (Figure 6).

**Table 5.** Areal means of PW–AVG (mm), standard deviation of PW–SD (mm) and variability coefficient of PW–VC (%) between 1983–2010.

	I	II	III	IV	V	VI	VII	VIII	IX	X	XI	XII	Annual
AVG	8.7	8.6	9.7	12.9	18.5	22.6	25.8	25.2	20.1	15.7	12.1	9.6	15.8
SD	4.1	4.0	4.4	4.9	6.1	6.7	6.8	6.7	6.3	6.3	5.1	4.4	8.3
VC	46.4	46.1	44.8	37.8	33.2	29.5	26.2	26.7	31.2	40.1	41.9	45.9	52.7

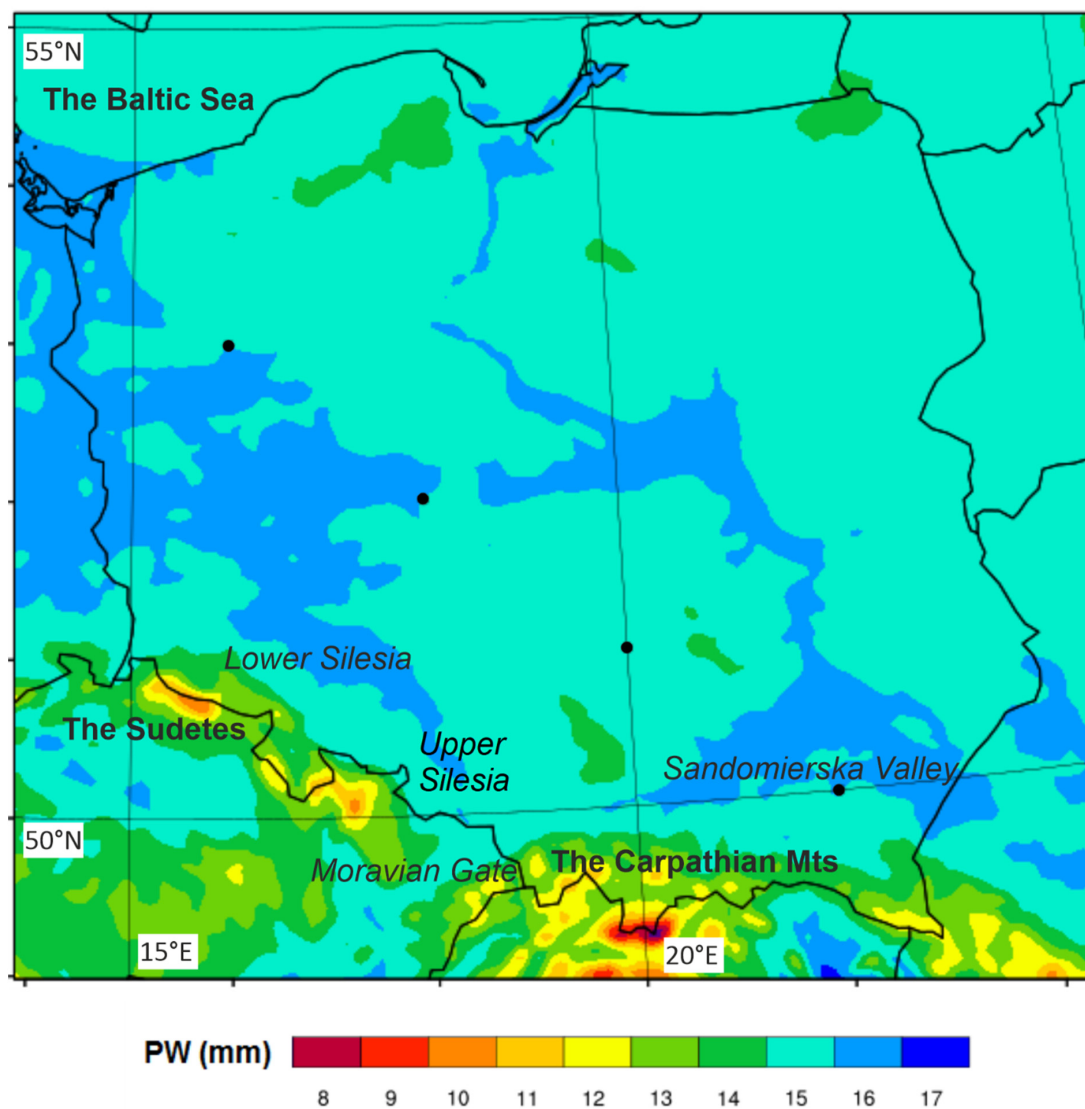


**Figure 5.** Annual PW value over Poland for the years 1983–2010. The black points indicate the places used in trend analysis.

PW over Poland shows a strong annual cycle, which is primarily a consequence of the annual course of air temperature (Table 5 and Figure 7). Hence, the areal mean PW is the highest in July (25.8 mm) and is three times lower (8.6 mm) in February. The standard deviations of PW in winter, late autumn and early spring months are high, which causes areal variability coefficients (VC) to exceed 40%. In summer months, areal VC does not exceed 30%. In winter, the monthly mean of PW decreases over Poland from the west to the east. From May to August, there are specific regions of increased PW in the south-eastern and eastern parts of Poland except for the Carpathian Mountains, and in the land strip ranging from Lower Silesia to Silesia and the Moravian Gate. The PW variability coefficient shows a tendency to increase spatially from the west to the east, particularly in winter and autumn months. It corresponds to the decreasing amount of moisture carried from the Atlantic Ocean and small spatial variability of the PW standard deviation over Poland during prevalent advection from the west. In spring and summer the vs. increases from the south-west to the north-east (Figure 8). In spring and, to a smaller extent, in summer, during increased frequency of advection of relatively dry air from the NE sector in Poland, the larger PW standard deviations are observed in NE Poland. In summer, the average values of PW are higher in the southern and south-western part of Poland.

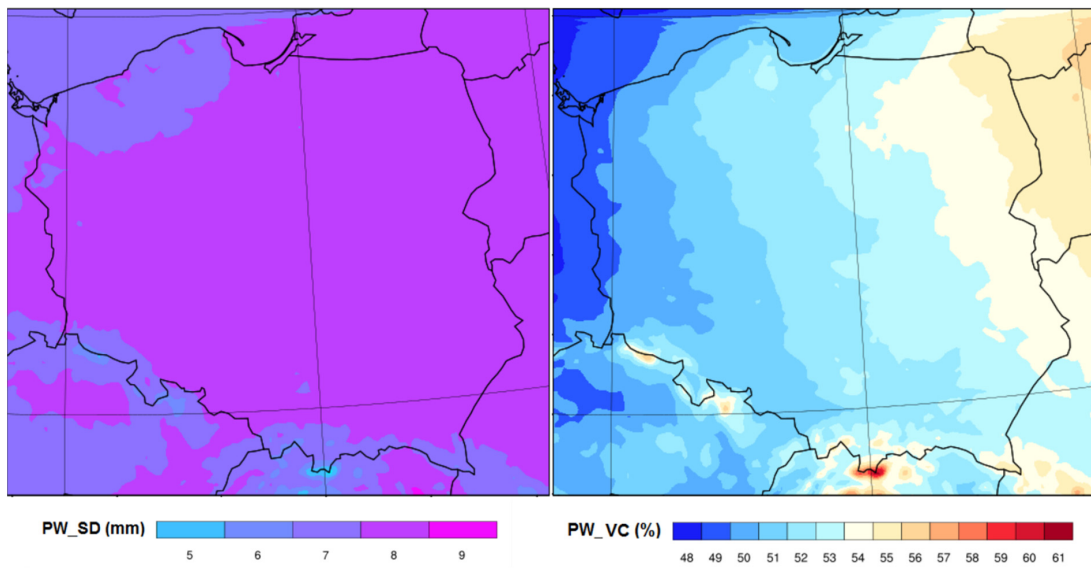


**Figure 6.** Standard deviation (left) and variability coefficient (right) of PW annual value over Poland for the years 1983–2010.

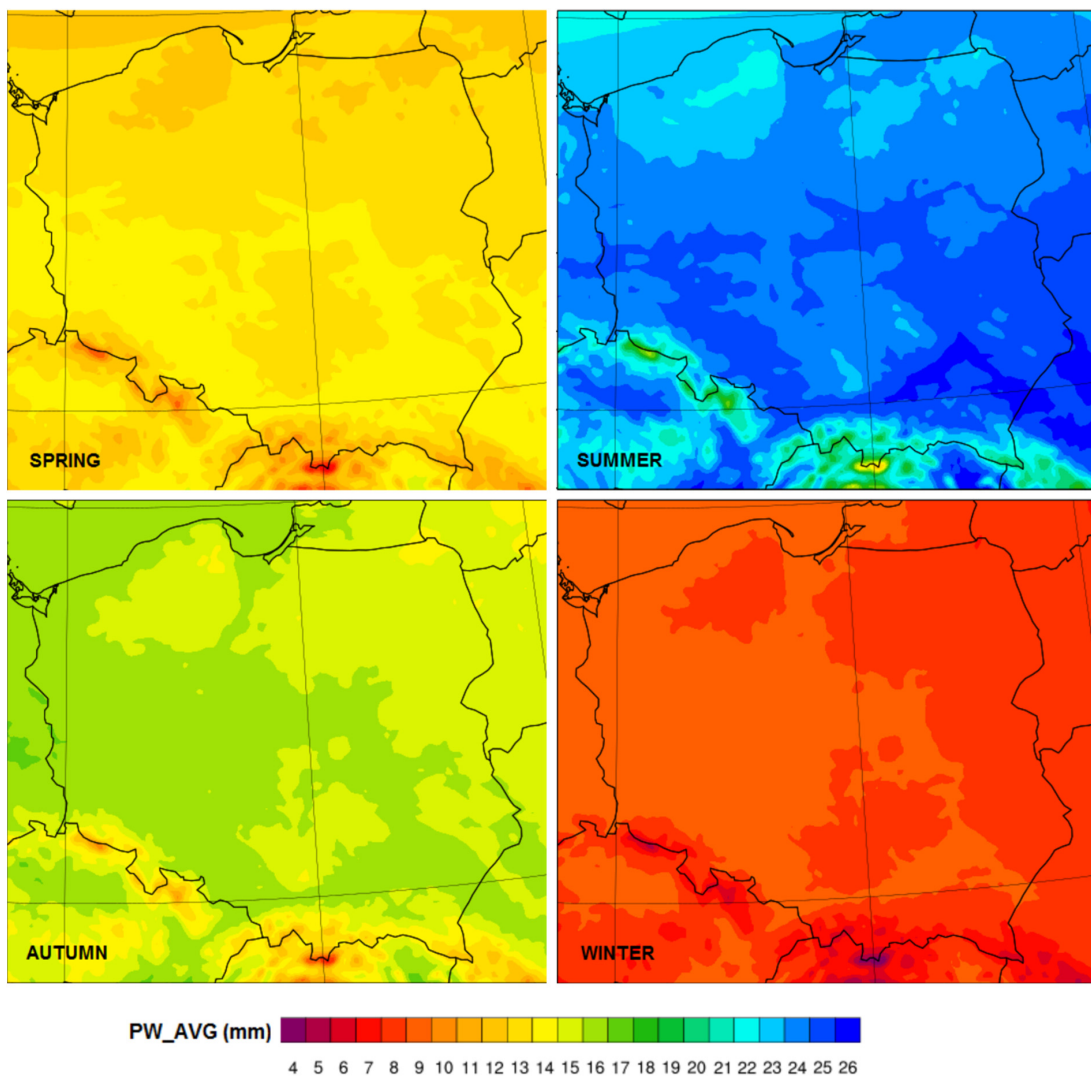


**Figure 7.** PW seasonal values (mm) over Poland for the years 1983–2010.

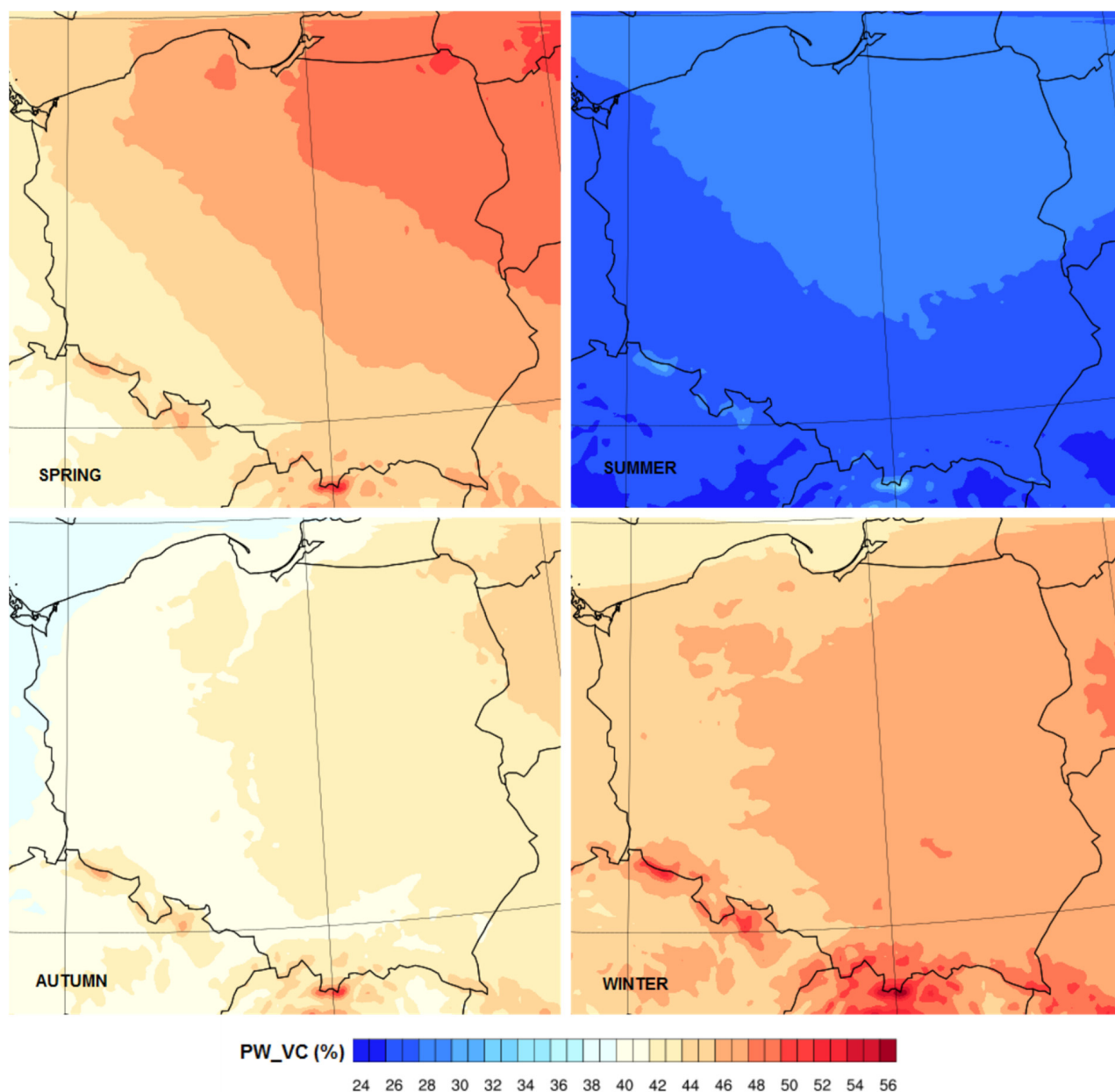


**Figure 8.** Variability coefficient (%) of PW seasonal value over Poland.

### 3.3. Spatial Distribution of PW over Poland at Individual Levels

Water vapor content decreases with height in the troposphere, and therefore the total annual precipitable water content from individual levels differs over the area of Poland from 8.2 mm (areal mean) at the level up to 1.5 km to 0.6 mm at the level of 6.0 to 10.0 km (Table 6). At lower levels of the troposphere, the spatial variability of PW is under significant influence of the orography. Up to 1.5 km, this influence is overlapped by the impact of the variable thickness of the analyzed troposphere level (Figure 9). Above this level, the smallest PW values are noted over convex terrain forms and the level of 1.5 to 3.0 km, where spatial differences between mean values of PW above mountainous areas reaches 3 mm. In the highest part of the troposphere, above 6.0 km, the mean value of PW and its spatial differences over the whole area of Poland does not exceed 1 mm.

**Table 6.** Areal seasonal and multi-year means of PW–AVG (mm), standard deviation of PW–SD (mm) and variability coefficient of PW–VC (%) for individual tropospheric levels.

		Up to 1.5 km	1.5–3 km	3–6 km	6–10 km
AVG	1983–2010	8.2	5.2	3.3	0.6
	Spring	7.3	4.5	2.7	0.4
	Summer	12.5	8.2	5.2	1.0
	Autumn	8.2	5.1	3.5	0.7
	Winter	4.7	2.9	1.9	0.3
SD	1983–2010	3.9	3.2	2.4	0.5
	Spring	3.0	2.6	1.8	0.3
	Summer	2.7	3.0	2.7	0.6
	Autumn	3.0	2.8	2.2	0.5
	Winter	1.9	1.8	1.3	0.2
VC	1983–2010	47.6	61.5	72.7	83.3
	Spring	41.1	57.8	66.7	75.0
	Summer	21.6	36.6	51.9	60.0
	Autumn	36.6	54.9	62.9	71.4
	Winter	40.4	62.1	68.4	66.7

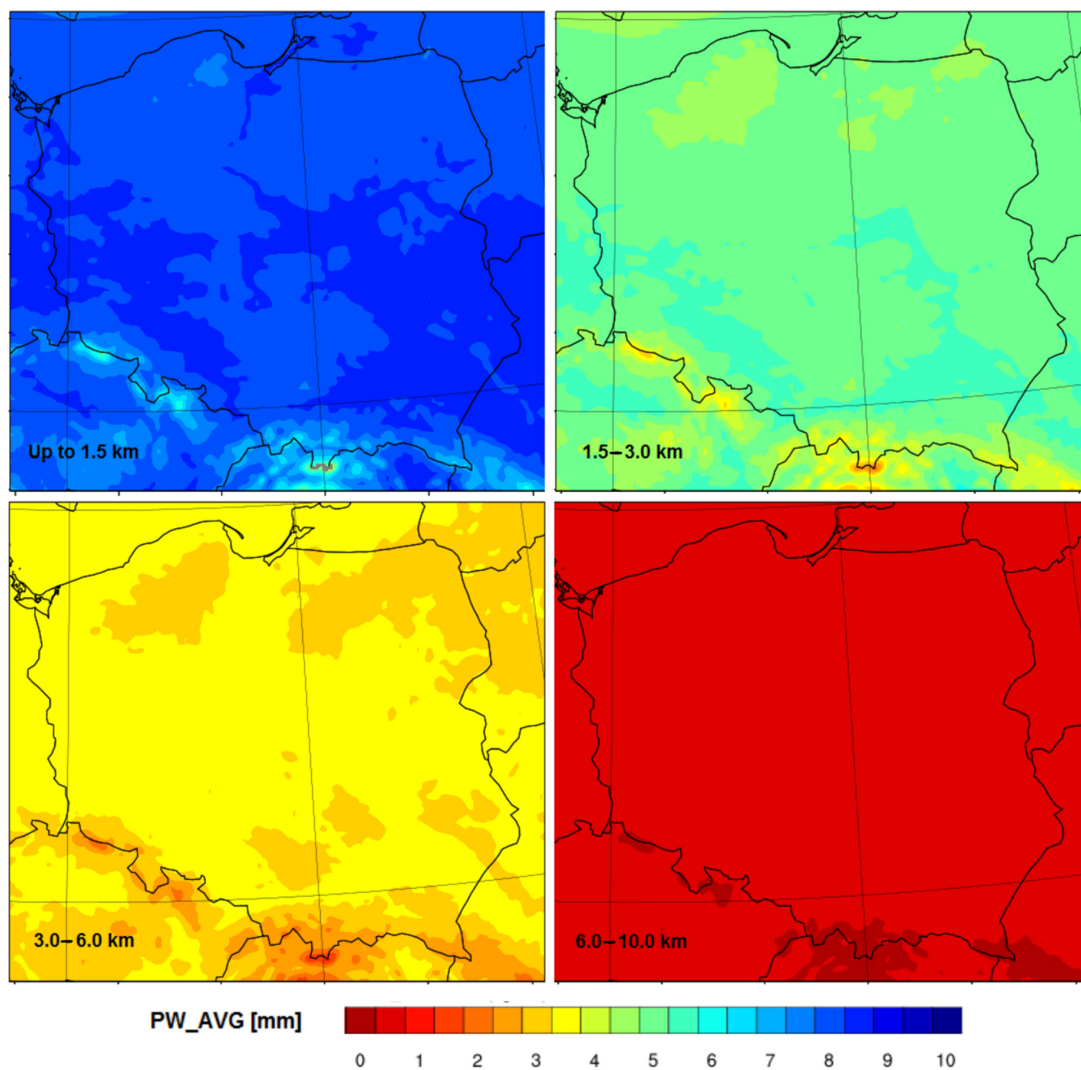


**Figure 9.** PW annual values (mm) from the years 1981–2010 over Poland at individual levels: up to 1.5 km, 1.5–3 km, 3–6 km and 6–10 km. Grids excluded from the analysis are in gray.

The standard deviation of PW at individual levels related to average values increases with height (Table 6). Except for the mountainous areas, the spatial variability of SD at the level of below 1.5 km increases from the west to the east, which is also linked to the changes of the PW variability coefficient (Figure 10), especially in autumn and winter. In the upper levels of the troposphere, PW increases from the south-west to the north-east, almost regardless of the season. In the north-eastern parts of Poland, the VC at the level of 6.0 to 10.0 km reaches 85%. In the lower part of the troposphere, the VC does not exceed 60%.

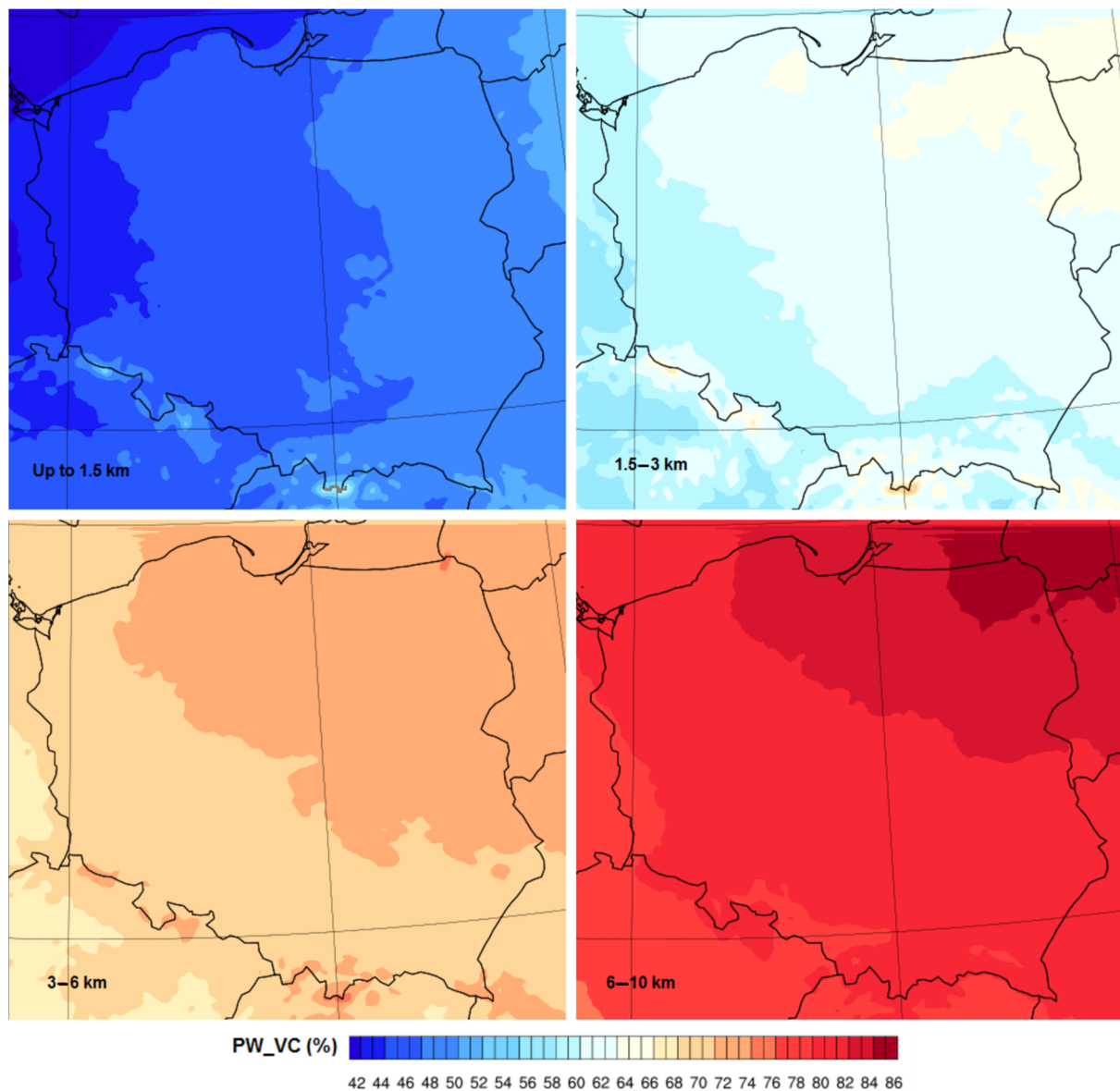


**Figure 10.** PW variability coefficient (%) between 1981 and 2010 over Poland at individual levels: up to 1.5 km, 1.5–3 km, 3–6 km and 6–10 km. Grids excluded from the analysis are in gray.

The seasonal changes of the areal mean of PW at individual tropospheric levels are similar in the whole column of the troposphere, with the highest values in summer and the lowest in winter (Table 6). Regardless of the height of the tropospheric layer, the values of the areal standard deviation of PW related to average values are the smallest in summer. The highest value of standard deviation is noted in spring at the level up to 1.5 km and above 6 km, whereas in other layers it is observed in winter. The largest spatial diversity of the PW is observed at the levels up to 3 km in summer with the highest PW observed in the western and south-western parts of Poland with a characteristic belt along mountain ranges

with orographic dips such as the Moravian Gate or the Sandomierska Basin (Figure 11). Excluding mountainous areas in autumn and spring, the spatial diversity of PW values up to 3 km above Poland does not exceed 1.5 mm, whereas in winter and at higher altitudes, it reaches 0.5 mm.

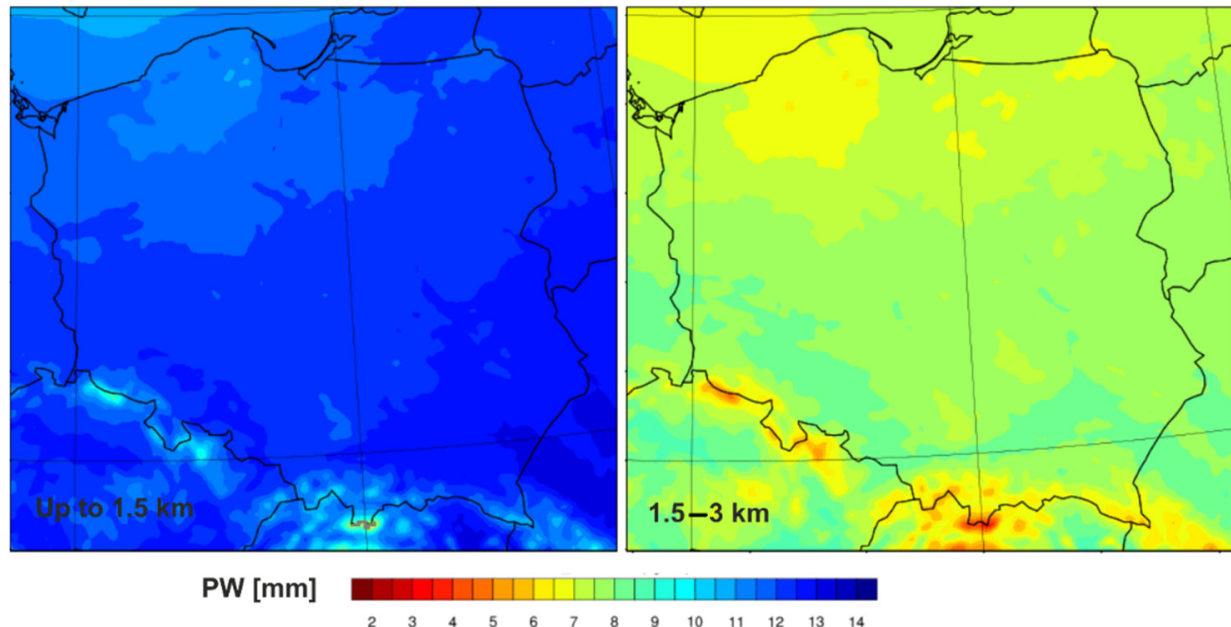


**Figure 11.** PW summer values (mm) at the level up to 1.5 km and from 1.5 to 3.0 km over Poland. Grids excluded from the analysis are in gray.

### 3.4. Trends of PW Changes

An upward tendency in annual PW values was observed in the vast majority of Poland between 1983 and 2010, but the trend is not statistically significant (Figure 12A). A statistically significant trend is noted only in the south-eastern parts of Poland at the tropospheric level up to 1.5 km. The Sen's slope does not exceed the value of 0.01. The period of the highest increase relates to the years 1996–2002 and after 2005. However, clear differences are observed in PW values between seasons and also between tropospheric layers.

Mostly in summer, an upward trend in PW seasonal mean in the whole column of the troposphere is noted, with the highest value of Sen's slope exceeding 0.08 over the entire area of Poland (Figure 12C). The trend is mainly observed from the south-western to the southern parts of Poland, and locally in the north (Figure 13). This tendency is observed also at the tropospheric level up to 1.5 km and between 1.5 and 3 km, but the range of the significant trend and Sen's slope is different (Figure 14A,B). At the level up to 1.5 km in the northern part of Poland, Sen's slope reaches to 0.05.

For spring, the trend of PW seasonal mean for the years 1983–2010 decreases over the whole area of Poland but is significant only in the northern part of the country (Figure 13). Locally, the Sen's slope reaches  $-0.06$ . A decreasing tendency is calculated for all lower levels of the troposphere, but the most apparent trend is noted between 1.5 and 3 km in the northern and north-eastern parts of Poland (Figure 14C,D). This trend is observed locally also in the layer from 3 to 6 km. The strongest decrease in spring PW mean was observed between the years 1986 and 1987 (Figure 12B).

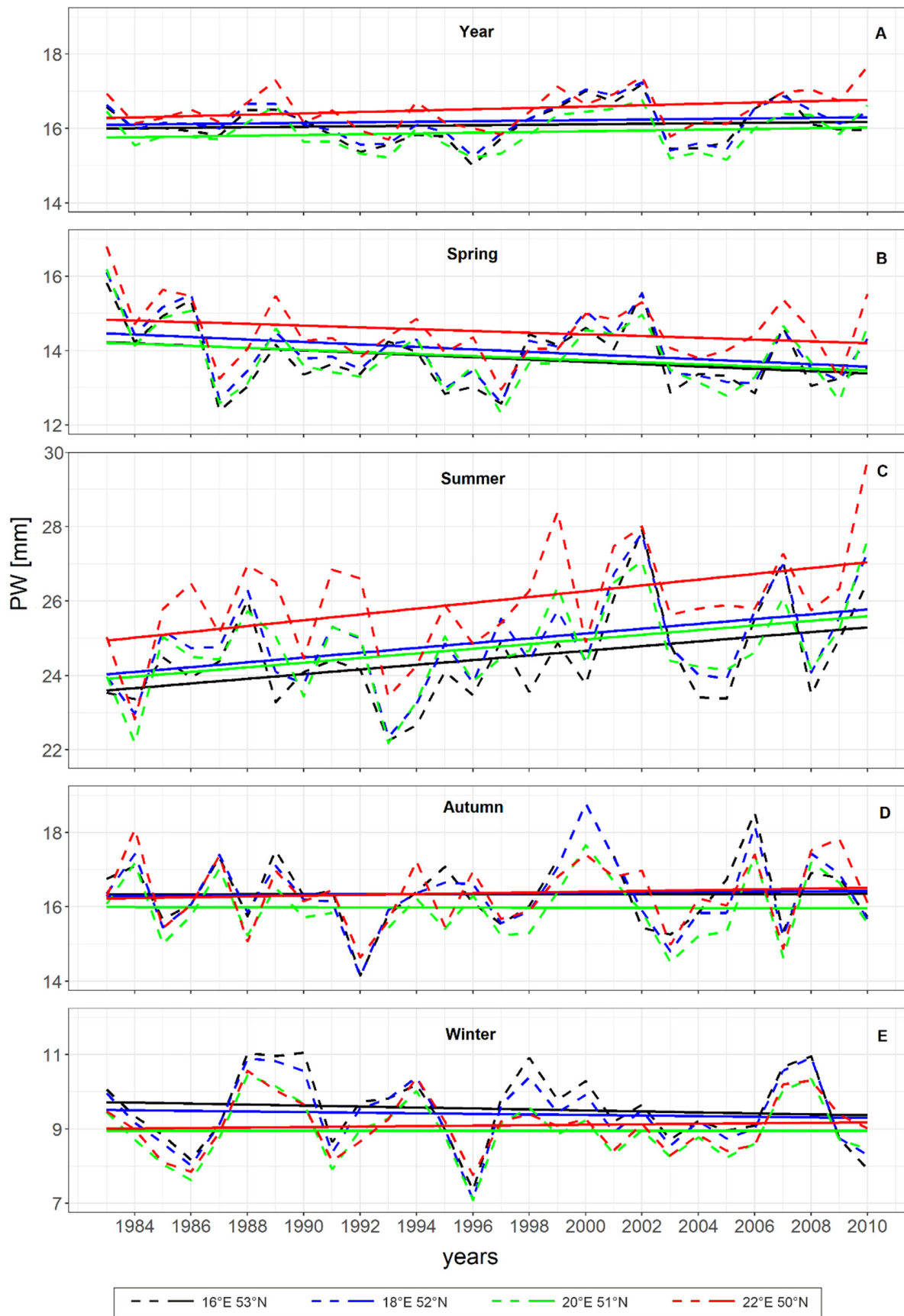


**Figure 12.** Annual (A) and seasonal (B–E) PW (dashed lines) with trend lines (solid lines) for selected grid points from the years 1983–2010.

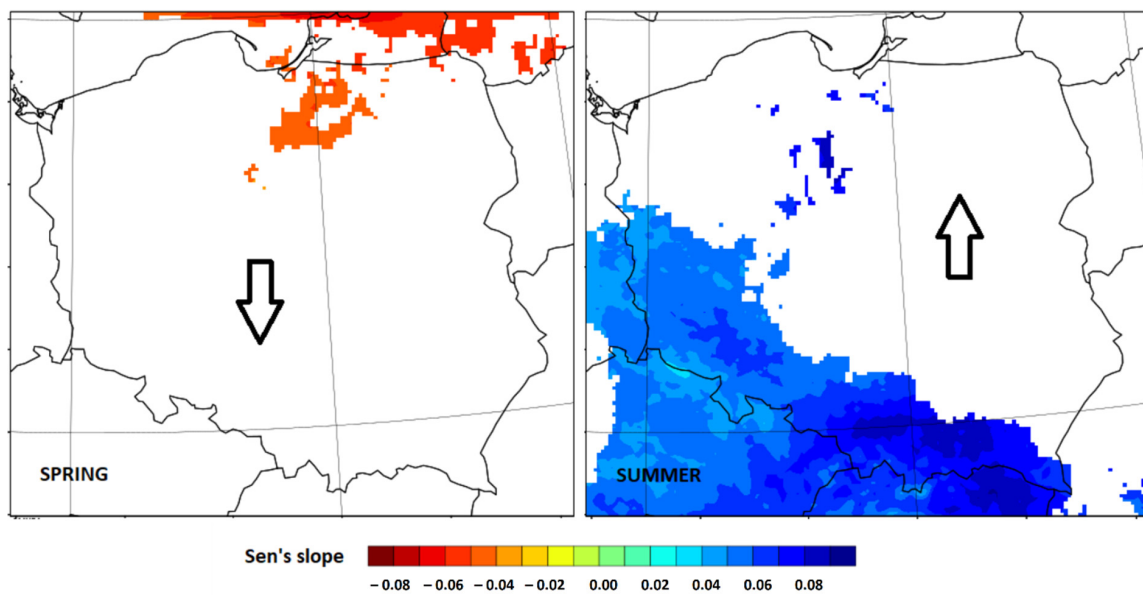


**Figure 13.** Sen's slope for significant trends ( $\alpha = 0.05$ ) of average spring and summer PW over Poland in the years 1983–2010. The arrows show direction of PW changes over the area of Poland without statistically significant trends.

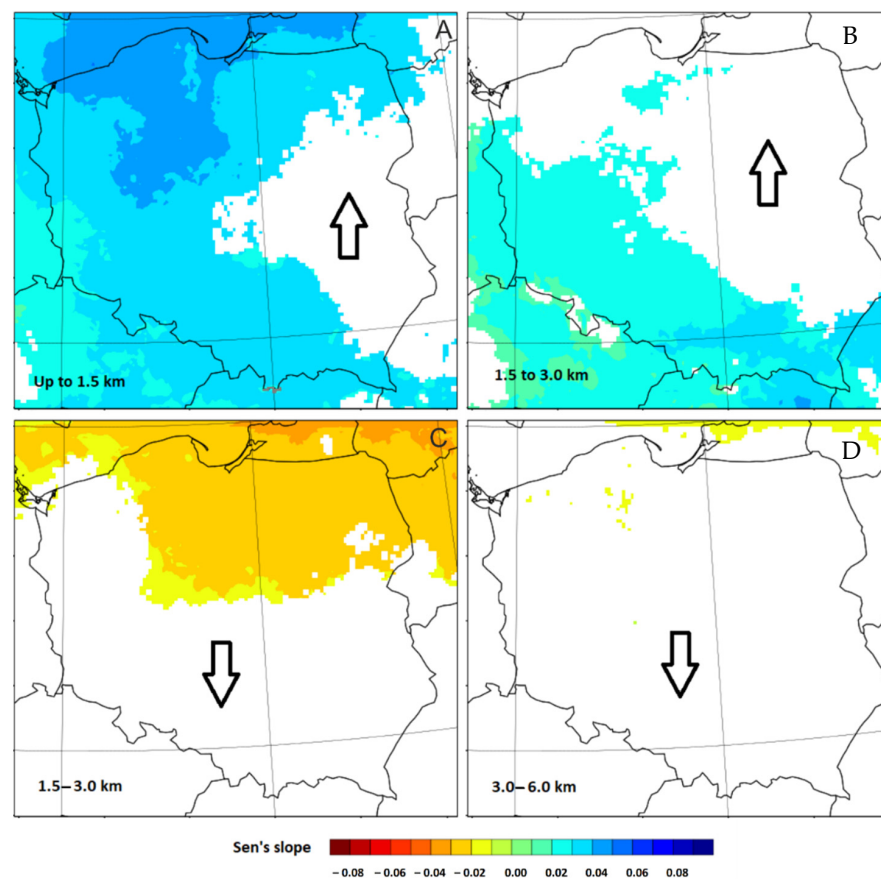


**Figure 14.** Sen's slope for significant trends ( $\alpha = 0.05$ ) of average summer PW at the level up to 1.5 km (A) and from 1.5 to 3.0 km (B) and average spring PW at the level from 1.5 to 3 km (C) and from 3 to 6 km (D) over Poland in the years 1983–2010. The arrows show the direction of PW changes over the area of Poland without statistically significant trends. Excluded grid points with altitude over 1.5 km above sea level are marked in gray.

There is no statistically significant tendency in mean PW for autumn over the area of Poland. A small PW increase is noted up to 1.5 km in the troposphere, but above 1.5 km in the north-western part of Poland, the tendency is negative. The highest increase in this PW seasonal mean was recorded at the end of the 20th century. However, it was followed by a significant decrease (Figure 12D). There is no statistically significant tendency in PW seasonal mean for winter, but regardless of the analyzed tropospheric layer, the direction of PW tendency is changing over the area of Poland from negative in the north-west to positive in the south-east. The highest PW winter mean variability relates to the years 1986–1998 (Figure 12E).

The increase in annual maximum values of PW is observed also over Poland. However, the trend for the years 1983–2010 is statistically significant only locally, mainly in the western and north-eastern part of the country (Figure 15). The Sen's slope of these trend lines reaches from 0.08 to 0.3. In an analyzed time series for selected points, only in 1996, the maximum value decreases below 40 mm. After that, the maximum values of PW reach and exceed 50 mm (Figure 16). The tendency of the areal annual maximum of the analyzed area is also positive but not statistically significant.

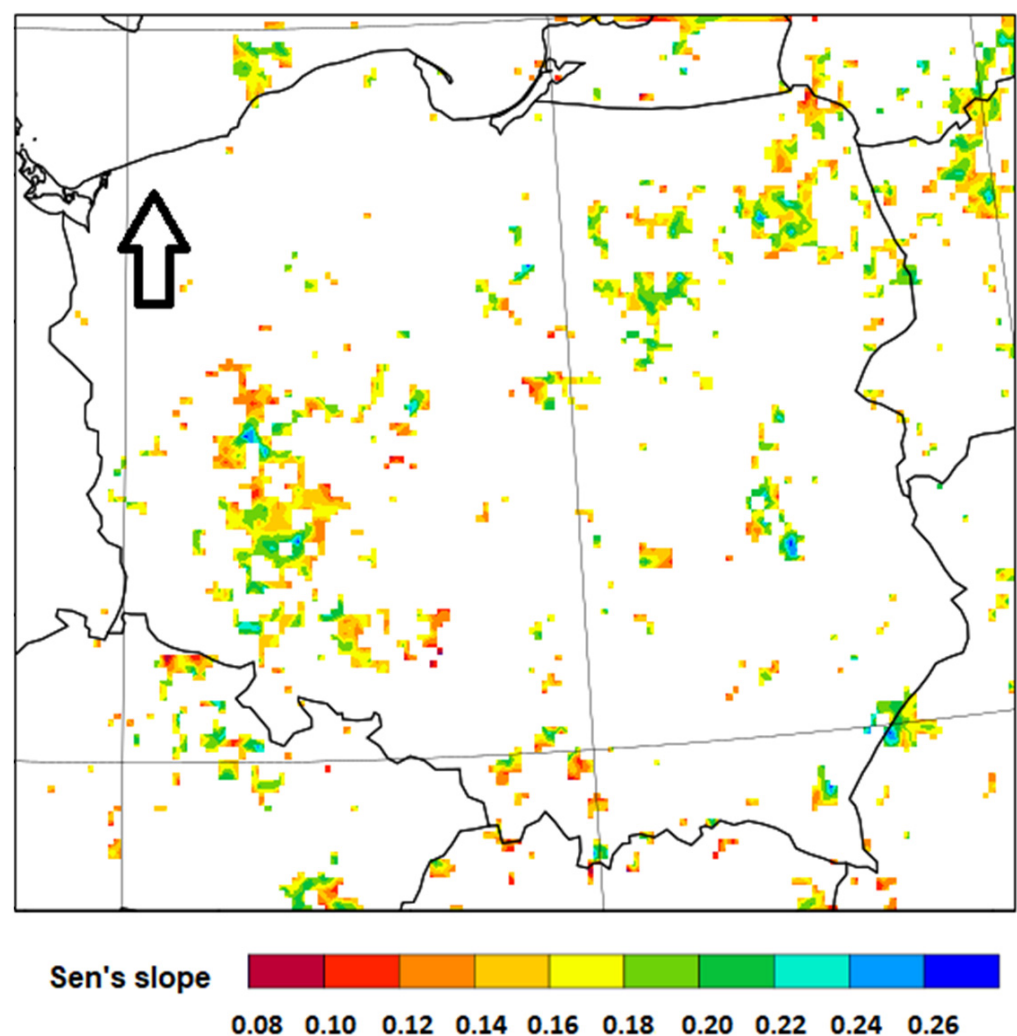


**Figure 15.** Sen's slope for significant trends ( $\alpha = 0.05$ ) of annual maximum value of PW. The arrow shows direction of changes of the annual maximum value of PW over the area of Poland without statistically significant trends.

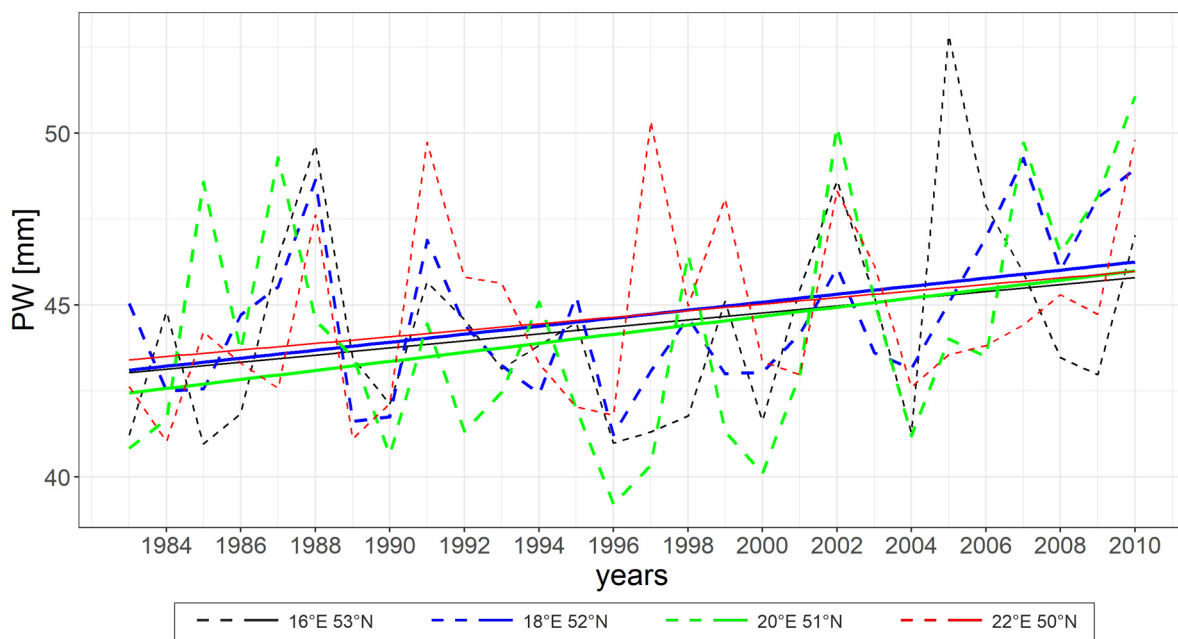


**Figure 16.** Annual maximum of PW (dashed lines) with trend lines (solid lines) for selected grid points from the years 1983–2010. Lines of statistically significant trends, and accordingly PW courses, are in bold.

#### 4. Discussion

In previous climatological studies on the column-integrated atmospheric water vapor (PW), covering the global or European scale, the main reanalysis data sources were ERA-40 [76], NCEP/NCAR [57,77–79], MERRA or MERRA2 [78,80], CFSR [80], ERA-Interim [35,77,80] and ERA-5 [81–83]. All of the mentioned studies emphasized the applicability of these kinds of data in spatial and temporal studies. In our study, the high-resolution reanalysis developed with the Weather Research and Forecasting model was applied for spatial–climatological analysis of precipitable water content over Poland. Evaluation of the modeled PW data showed good agreement with the PW from atmospheric soundings, especially if the whole column of the troposphere and the winter season are considered. In the analyzed period of 2001–2010, Pearson correlation coefficients reached 0.97 for the whole year and did not fall below 0.92 if seasonal PW was considered. These results are in agreement with those obtained by, e.g., González et al. [84], Fedele et al. [85], Pérez-Jordán et al. [23], Varga and Breuer [82] and Diaz et al. [86], where the authors reported close agreement of the whole column of PW values. In our work, a similar model configuration was used [23], which was tested in the earlier work of González et al. [84]. The configuration was also tested for the area of Poland for rainfall forecasting [64,65].

In this study, PW data derived with the mesoscale model WRF were evaluated not only in relation to the entire profile of the troposphere, but also for four individual layers in a vertical profile: below 1.5 km, from 1.5 to 3.0 km, from 3.0 to 6.0 km and from 6.0 to 10.0 km. The results show some differences in model–measurement agreement depending on the analyzed tropospheric level. The highest Pearson correlation coefficients and the smallest RMSE were observed for the level up to 1.5 km and from 3.0 to 6.0 km. Similar to other studies [23,87], the WRF model overestimated observed values of PW over the entire year. The highest overestimation and the highest RMSE, reaching 3.14 mm, were calculated for summer seasons. Moreover, the Pearson correlation coefficient in the summer months was the lowest for all analyzed tropospheric levels, but especially for the 1.5–3.0 km layer. This could be associated with a higher vertical temperature gradient, more intense air vertical mixing, and a higher condensation level with cloud base, which is typical for the period from May to August. Because of that, in the summer months in the 1.5–3.0 km layer,

dynamical processes within clouds are typical, and drop size distribution is highly variable in time and space, causing PW to vary as well [88].

It should also be noted that the differences between PW obtained from the WRF model and soundings may also result from the limitations associated with the soundings (the radiosonde ascent may take around 30–40 min to complete [89]). If PW from the WRF model is calculated in a vertical column representing the location of the sounding station, the PW from soundings takes into account the real (inclined) path along which the balloon rises. It matters especially for the highest part of troposphere, above 6 km. Additionally, radiosonde has a decreasing response to relative humidity at low temperatures. It also tends to underestimate water vapor near saturation [90]. However, when the troposphere is dry above low clouds, the effect is opposite.

The results of climatological analysis of PW are in line with previously presented areal mean values for Poland, which were obtained from NCEP/NCAR reanalysis [59] and from ERA-Interim reanalysis for Europe and North Atlantic [35]. However, our work presents high-resolution spatial variability of PW annual and seasonal values over Poland. It was shown here that in the lowest layer (up to 1.5 km), the spatial variability of PW is influenced by the altitude reducing the height of the analyzed air column. The impact of elevation on PW is especially strong for the layers above 1.5 km. The convex landforms generate additional cloudiness, either by forced pumping of inflowing air (throughout the year with autumn and winter maximum), or by creating convective cloudiness (summer-spring) over higher mountain ranges. These processes lead to the transition of vapor into water or ice and thus reduce PW. This effect could be particularly intense during the formation of orographic precipitation and to a lesser extent fog precipitation. In the analyzed area, the reduction in PW over mountains ranges is clear especially in the layer 1.5 to 3 km, not only over the area of cloud formation but also on the leeward side. A large decrease in PW with increasing altitude is more distinct in spring and summer compared to the winter season. It is associated with a higher vertical temperature gradient and a higher condensation level with a cloud base in the warmer half of the year as well as higher intensity and frequency of cloud formation and precipitation via the transformation rate from water vapor over mountainous regions [91].

We showed in our work that outside the mountainous area, the annual and seasonal averages of PW vary within a narrow range. However, some significant differences between seasonal spatial distributions were larger especially in 1.5 to 3 km level. For winter and autumn, the PW values were increasing from east to west. This confirms the role of the western circulation in water vapor distribution in Europe, as described by Zveryaev et al. [79] and Wypych et al. [35]. In spring and summer during the more frequent southern atmospheric advection, the highest PW values are noted in the south-eastern part of Poland. This is due to the fact that the transport of moist air is affected by the Carpathians and the Sudety Mountains. It also suggests the importance of the airflow in existing openings: in orographic dip channels (e.g., the Moravian Gate, the Sandomierska Valley) or around the entire block of the Carpathians and the Sudetes. In a similar way, the moist tropical air moves from the south through the gap between the Massif Central and the Alps, then along Saonne and Rhein valleys [28]. The higher variability of PW at the lower tropospheric level in summer months confirms also the significant impact of temperature and convection, which is in line with work of Wypych et al. [35]. Local production of significant quantities of water vapor occurs due to more intense evaporation from vegetation, moist soil and water bodies [92].

Our study shows an increasing trend of PW annual values between 1983 and 2010, but the trend is statistically insignificant. In addition, a locally significant increasing tendency of annual maximum values of PW is proved. Comparison with other results from the literature is difficult due to different study periods. However, some conclusions from previous articles are in line with our results. Wibig and Siedlecki [57], based on NCEP/NCAR reanalysis for the years of 1958 to 2005, underline that negative trends of PW annual means are recorded over the western parts of Europe, whereas positive ones

are recorded over its eastern parts. Although their analysis concerned a longer period, they identified a low tendency of PW changes over the area of Poland (the linear trend of PW annual values is close to 0) and also the fact that statistically significant changes are observed only locally. Earlier results from Trenberth et al. [76] for years 1988–2001 (based on NCEP and ERA-40 reanalysis) show that trend of PW annual means over Europe has no evident direction and does not exceed 0.5 mm per decade. This is also in agreement with observations from Europe by Ross and Elliott [93]. Recent studies on PW trends for stations in Finland showed no significant trend until 2010. For the next decade, there was a sharp and significant increasing trend [94].

Our study showed a significant positive trend with a high Sen's slope for the summer season up to 3 km in the troposphere. A significant but negative tendency was noted also for spring in the northern part of Poland, whereas for autumn and winter the trends were insignificant. For winter, the direction of changes varied spatially from negative in the north-west to positive in the south-east. Wibig and Siedlecki [57] also found seasonal changes in PW variability over the area of Poland and Central Europe. Contrary to our results, Degirmendžić and Kożuchowski [60] using NCEP/NCAR reanalysis in the years of 1958 to 2008 found only negative trends of PW values in seasons, but the observed tendencies were significant only for spring and autumn. However, their results summarized longer period and related to the mean PW values from six grid points ( $2.5^\circ \varphi \times 2.5^\circ \lambda$ ), whereas in our study, trends were calculated separately for each  $5 \text{ km} \times 5 \text{ km}$  grid cell in Poland. It may be assumed that multi-year and multi-seasonal changes of PW are related to changes in the atmospheric circulation, but this requires further analysis.

## 5. Conclusions

In this work we show that:

- PW calculated with the high-resolution WRF model meteorological data is in good agreement with data from atmospheric soundings. This is true not only for the entire column of the atmosphere but also for individual tropospheric levels. The closest agreement is observed in the lower part of the troposphere, especially for winter months.
- High-resolution PW information reveals detailed spatial and temporal variability over the area of Poland.
- Multi-year trends of PW variability are in line with previous studies, and the moisture content changes over Poland and Central Europe and contributes to the ongoing discussion on the observed climate changes.

**Author Contributions:** Conceptualization, H.O. and M.B.; methodology, H.O., M.B. and M.K.; software, H.O., M.B. and M.K.; validation, H.O.; formal analysis, H.O. and M.B.; investigation, H.O. and M.B.; resources, H.O., M.B. and M.K.; data curation, H.O., M.B. and M.K.; writing—original draft preparation, H.O. and M.B.; writing—review and editing, H.O., M.B. and M.K.; visualization, H.O.; supervision, H.O. and M.B.; project administration, H.O. and M.B.; funding acquisition, M.B. All authors have read and agreed to the published version of the manuscript.

**Funding:** This research was funded by National Science Centre project no. UMO-2015/17/B/ST10/03827. The computational work has been executed by the Wrocław Centre of Networking and Supercomputing (<http://www.wcss.wroc.pl> accessed on 2 January 2021, grant no. 170). The study was supported by the European Union's Horizon 2020 research and innovation program under grant agreement No. 856599.

**Institutional Review Board Statement:** Not applicable.

**Informed Consent Statement:** Not applicable.

**Data Availability Statement:** Not applicable.

**Conflicts of Interest:** One of authors (Maciej Kryza) is a member of the Editorial Board. The authors declare no others conflict of interest.

## References

1. Glossary of Meteorology—AMS—American Meteorological Society. Precipitable Water. Available online: [http://glossary.ametsoc.org/wiki/Precipitable\\_water](http://glossary.ametsoc.org/wiki/Precipitable_water) (accessed on 16 May 2020).
2. Bordi, I.; Zhu, X.; Fraedrich, K. Precipitable water vapour and its relationship with the Standardized Precipitation Index, ground based GPS measurements and reanalysis data. *Theor. Appl. Climatol.* **2016**, *123*, 263–275. [[CrossRef](#)]
3. Tuller, S.E. Seasonal and annual precipitation efficiency in Canada. *Atmosphere* **1973**, *11*, 52–66. [[CrossRef](#)]
4. Fadil, A.; Ben Sari, D. Correlation between precipitable water and rainfall using global positioning system (GPS) technique. In *Remote Sensing of the Atmosphere for the Environmental Security*; Perrin, A., Ben Sari-Ziz, N., Demaison, J., Eds.; NATO Security through Science Series (NATO Security through Science Series C, Environmental Security); Springer: Dordrecht, The Netherlands, 2006; pp. 271–284.
5. Ye, H.; Fetzer, E.J.; Wong, S.; Behrangi, A.; Olsen, E.T.; Cohen, J.; Lambrigtsen, B.H.; Chen, L. Impact of increasing water vapour on precipitation efficiency over northern Eurasia. *Geophys. Res. Lett.* **2014**, *41*, 2941–2947. [[CrossRef](#)]
6. Chakraborty, S.; Adhikari, A.; Maitra, A. Rainfall estimation from liquid water content and precipitable water content data over land; ocean and plateau. *Atmos. Res.* **2016**, *167*, 265–274. [[CrossRef](#)]
7. Gueymard, C.A. Impact of on-site atmospheric water vapor estimation methods on the accuracy of local solar irradiance predictions. *Sol. Energy* **2014**, *101*, 74–82. [[CrossRef](#)]
8. Bright, J.M.; Gueymard, C.A.; Killinger, S.; Lingfors, D.; Sun, X.X.; Wang, P.; Engerer, N.A. Climatic and Global Validation of Daily MODIS Precipitable Water Data at AERONET Sites for Clear-sky Irradiance Modelling. In Proceedings of the ISES EuroSun 2018 Conference—12th International Conference on Solar Energy for Buildings and Industry, Rapperswil-Jona, Switzerland, 13 September 2018; pp. 1490–1501. [[CrossRef](#)]
9. Obregon, M.A.; Serrano, A.; Costa, M.J.; Silva, A.M. Global Spatial and Temporal Variation of the Combined Effect of Aerosol and Water Vapour on Solar Radiation. *Remote Sens.* **2021**, *13*, 708. [[CrossRef](#)]
10. Salamalikis, V.; Vamvakas, I.; Gueymard, C.A.; Kazantzidis, A. Atmospheric water vapor radiative effects on shortwave radiation under clear skies: A global spatiotemporal analysis. *Atmos. Res.* **2021**, *251*, 105418. [[CrossRef](#)]
11. Kelsey, V.; Riley, S.; Minschwaner, K. Atmospheric precipitable water vapor and its correlation with clear-sky infrared temperature observations. *Atmos. Meas. Technol.* **2022**, *15*, 1563–1576. [[CrossRef](#)]
12. Ruckstuhl, C.; Philipona, R.; Morland, J.; Ohmura, A. Observed relationship between surface specific humidity, integrated water vapor, and longwave downward radiation at different altitudes. *J. Geophys. Res. Atmos.* **2007**, *112*, D03302. [[CrossRef](#)]
13. Naud, C.M.; Miller, J.R.; Landry, C. Using satellites to investigate the sensitivity of longwave downward radiation to water vapor at high elevations. *J. Geophys. Res. Atmos.* **2012**, *117*, D05101. [[CrossRef](#)]
14. Maghrabi, A.H.; Almutayri, M.M.; Aldosary, A.F.; Allehyani, B.I.; Aldakhil, A.A.; Aljarba, G.A.; Altilasi, M.I. The influence of atmospheric water content, temperature, and aerosol optical depth on downward longwave radiation in arid conditions. *Theor. Appl. Climatol.* **2019**, *138*, 1375–1394. [[CrossRef](#)]
15. Hao, M.J.; Lin, Y.L.; Luo, Y.; Nath, R.; Zhao, Z.C. The impact of atmospheric moisture transport on winter Arctic warming: Radiation versus latent heat release. *Int. J. Climatol.* **2021**, *41*, 3982–3993. [[CrossRef](#)]
16. Harvey, L.D.D. An assessment of the potential impact of a downward shift of tropospheric water vapor on climate sensitivity. *Clim. Dyn.* **2000**, *16*, 491–500. [[CrossRef](#)]
17. Colman, R. Geographical contributions to global climate sensitivity in a General Circulation Model. *Glob. Planet. Chang.* **2002**, *32*, 211–243. [[CrossRef](#)]
18. Zhang, J.P.; Zhao, T.B. Historical and future changes of atmospheric precipitable water over China simulated by CMIP5 models. *Clim. Dyn.* **2019**, *52*, 6969–6988. [[CrossRef](#)]
19. Virginie, M.; Jean-François, M. Four-Dimensional Variational Assimilation of Total Column Water Vapor in Rainy Areas. *Mon. Weather Rev.* **2002**, *130*, 43–58. [[CrossRef](#)]
20. Meng, Z.; Yunqi, N.; Fuqing, Z. Variational assimilation of GPS precipitable water vapor and hourly rainfall observations for a meso- $\beta$  scale heavy precipitation event during the 2002 mei-yu season. *Adv. Atmos. Sci.* **2007**, *24*, 509–526. [[CrossRef](#)]
21. Takuya, K.; Tohru, K.; Hiromu, S.; Kazuo, S. Cloud-Resolving 4DVAR Assimilation Experiment for a Local Heavy Rainfall Event in the Tokyo Metropolitan Area. *Mon. Weather Rev.* **2011**, *139*, 1911–1931. [[CrossRef](#)]
22. Moore, A.; Small, I.J.; Gutman, S.; Laber, J. National weather service forecasters use GPS precipitable water vapor for enhanced situational awareness during the southern California summer monsoon. *Bull. Am. Meteorol. Soc.* **2015**, *96*, 1867–1877. [[CrossRef](#)]
23. Pérez-Jordán, G.; Castro-Almazán, J.A.; Muñoz-Tuñón, C.; Codina, B.; Vernin, J. Forecasting the precipitable water vapour content, validation for astronomical observatories using radiosoundings. *Mon. Not. R. Astron. Soc.* **2015**, *452*, 1992–2003. [[CrossRef](#)]
24. Risanto, C.B.; Castro, C.L.; Moker, J.M., Jr.; Arellano, A.F., Jr.; Adams, D.K.; Fierro, L.M.; Minjarez Sosa, C.M. Evaluating Forecast Skills of Moisture from Convective-Permitting WRF-ARW Model during 2017 North American Monsoon Season. *Atmosphere* **2019**, *10*, 694. [[CrossRef](#)]
25. Zhao, Q.Z.; Liu, Y.; Yao, W.Q.; Yao, Y.B. Hourly Rainfall Forecast Model Using Supervised Learning Algorithm. *IEEE Trans. Geosci. Remote Sens.* **2022**, *60*, 1–9. [[CrossRef](#)]
26. Ikuta, Y.; Seko, H.; Shoji, Y. Assimilation of shipborne precipitable water vapour by Global Navigation Satellite Systems for extreme precipitation events. *Q. J. R. Meteorol. Soc.* **2022**, *148*, 57–75. [[CrossRef](#)]
27. Dotzek, N. An updated estimate of tornado occurrence in Europe. *Atmos. Res.* **2003**, *67–68*, 153–161. [[CrossRef](#)]

28. Bissolli, P.; Grieser, J.; Dotzek, N.; Welsch, M. Tornadoes in Germany 1950–2003 and their relation to particular weather conditions. *Glob. Planet Chang.* **2007**, *57*, 124–138. [[CrossRef](#)]
29. Sobik, M.; Błaś, M. Wyjątkowe zdarzenia meteorologiczne. In *Wyjątkowe Zdarzenia Przyrodnicze na Dolnym Śląsku*; Migoń, P., Ed.; University of Wrocław: Wrocław, Poland, 2010; pp. 35–59. (In Polish)
30. Allan, R.P.; Lavers, D.A.; Champion, A.J. Diagnosing links between atmospheric moisture and extreme daily precipitation over the UK. *Int. J. Climatol.* **2016**, *36*, 3191–3206. [[CrossRef](#)]
31. Bonafoni, S.; Biondi, R.; Brenot, H.; Anthes, R. Radio occultation and ground-based GNSS products for observing, understanding and predicting extreme events, a review. *Atmos. Res.* **2019**, *230*, 104624. [[CrossRef](#)]
32. Hagos, S.M.; Leung, R.L.; Garuba, O.A.; Demott, C.; Harrop, B.; Lu, J.; Ahn, M.S. The Relationship between Precipitation and Precipitable Water in CMIP6 Simulations and Implications for Tropical Climatology and Change. *J. Clim.* **2021**, *34*, 1587–1600. [[CrossRef](#)]
33. Kim, S.; Sharma, A.; Wasko, C.; Nathan, R. Linking Total Precipitable Water to Precipitation Extremes Globally. *Earths Future* **2022**, *10*, e2021EF002473. [[CrossRef](#)]
34. Mishra, A.K. Variability of integrated precipitable water over India in a warming climate. *Meteorol. Appl.* **2020**, *27*, e1869. [[CrossRef](#)]
35. Wypych, A.; Bochenek, B.; Różycki, M. Atmospheric Moisture Content over Europe and the Northern Atlantic. *Atmosphere* **2018**, *9*, 18. [[CrossRef](#)]
36. Neiman, P.J.; Ralph, F.M.; Wick, G.A.; Lundquist, J.D.; Dettinger, M.D. Meteorological characteristics and overland precipitation impacts of atmospheric rivers affecting the West Coast of North America based on eight years of SSM/I satellite observations. *J. Hydrometeorol.* **2008**, *9*, 22–47. [[CrossRef](#)]
37. Browning, K.A. Organization of clouds and precipitation in extratropical cyclones. In *Extratropical Cyclones, The Erik Palmén Memorial Volume*; Newton, C.W., Holopainen, E., Eds.; American Meteorological Society: Boston, MA, USA, 1990; pp. 129–153.
38. Carlson, T.N. *Mid-Latitude Weather Systems*; Harper-Collins: London, UK, 1991.
39. Ralph, F.M.; Neiman, P.J.; Wick, G.A. Satellite and CALJET aircraft observations of atmospheric rivers over the eastern North Pacific Ocean during the winter of 1997/98. *Mon. Weather Rev.* **2004**, *132*, 1721–1745. [[CrossRef](#)]
40. Dettinger, M.; Ralph, F.M.; Das, T.; Neiman, P.J.; Cayan, D.R. Atmospheric rivers, floods and the water resources of California. *Water* **2011**, *3*, 445–478. [[CrossRef](#)]
41. Ramos, A.M.; Trigo, R.M.; Liberato, M.L.R.; Tome, R. Daily precipitation extreme events in the Iberian Peninsula and its association with Atmospheric Rivers. *J. Hydrometeorol.* **2015**, *16*, 579–597. [[CrossRef](#)]
42. Eiras-Barca, J.; Brands, S.; Miguez-Macho, G. Seasonal variations in North Atlantic atmospheric river activity and associations with anomalous precipitation over the Iberian Atlantic Margin. *J. Geophys. Res.-Atmos.* **2016**, *121*, 931–948. [[CrossRef](#)]
43. Eiras-Barca, J.; Ramos, A.M.; Algarra, I.; Vázquez, M.; Dominguez, F.; Miguez-Macho, G.; Nieto, R.; Gimeno, L.; Taboada, J.; Ralph, F.M. European West Coast atmospheric rivers, A scale to characterize strength and impacts. *Weather Clim. Extrem.* **2021**, *31*, 100305. [[CrossRef](#)]
44. Brands, S.; Gutiérrez, J.M.; San-Martín, D. Twentieth-century atmospheric river activity along the west coasts of Europe and North America: Algorithm formulation, reanalysis uncertainty and links to atmospheric circulation patterns. *Clim. Dyn.* **2017**, *48*, 9–10. [[CrossRef](#)]
45. Ross, R.J.; Elliott, W.P. Tropospheric water vapor climatology and trends over North America, 1973–1993. *J. Clim.* **1996**, *9*, 3561–3574. [[CrossRef](#)]
46. Durre, I.; Williams, C.N.; Yin, X.; Vose, R.S. Radiosonde-based trends in precipitable water over the Northern Hemisphere, an update. *J. Geophys. Res.* **2009**, *114*, D05112. [[CrossRef](#)]
47. Xie, B.; Zhang, Q.; Ying, Y. Trends in precipitable water and relative humidity in China, 1979–2005. *J. Appl. Meteorol. Clim.* **2011**, *50*, 1985–1994. [[CrossRef](#)]
48. Susskind, J.; Rosenfeld, J.; Reuter, D.; Chahine, M.T. Remote sensing of weather and climate parameters from HIRS2/MSU on TIROS-N. *J. Geophys. Res.* **1984**, *89*, 4677–4697. [[CrossRef](#)]
49. Malderen Van, R.; Brenot, H.; Pottiaux, E.; Beirle, S.; Hermans, C.; De Mazière, M.; Wagner, T.; De Backer, H.; Bruyninx, C. A multi-site intercomparison of integrated water vapour observations for climate change analysis. *Atmos. Meas. Technol.* **2014**, *7*, 2487–2512. [[CrossRef](#)]
50. Bevis, M.; Businger, S.; Chiswell, S.; Herring, T.; Anthes, R.; Rocken, C.; Ware, R. GPS Meteorology, Mapping Zenith Wet Delays onto Precipitable Water. *J. Appl. Meteorol.* **1994**, *33*, 379–386. [[CrossRef](#)]
51. Liang, H.; Cao, Y.; Wan, X.; Xu, Z.; Wang, H.; Hu, H. Meteorological applications of precipitable water vapour measurements retrieved by the national GNSS network of China. *Geod. Geodyn.* **2015**, *6*, 135–142. [[CrossRef](#)]
52. Fujita, M.; Sato, T. Observed behaviors of precipitable water vapour and precipitation intensity in response to upper air profiles estimated from surface air temperature. *Sci. Rep.* **2017**, *7*, 4233. [[CrossRef](#)]
53. Hanna, N.; Trzcina, H.N.; Möller, G.; Rohm, W.; Weber, R. Assimilation of GNSS tomography products into the Weather Research and Forecasting model using radio occultation data assimilation operator. *Atmos. Meas. Technol.* **2019**, *12*, 4829–4848. [[CrossRef](#)]
54. Ning, T.; Elgered, G.; European Space Agency. Monitoring Climate Using Ground-Based GNSS Measurements. Available online: [http://gssc.esa.int/navipedia/index.php/Monitoring\\_Climate\\_Using\\_Ground-based\\_GNSS\\_Measurements](http://gssc.esa.int/navipedia/index.php/Monitoring_Climate_Using_Ground-based_GNSS_Measurements) (accessed on 10 May 2015).

55. Niell, A.E.; Coster, A.J.; Solheim, F.S.; Mendes, V.B.; Toor, P.C.; Langley, R.B.; Upham, C.A. Comparison of measurements of atmospheric wet delay by radiosonde, water vapor radiometer, GPS, and VLBI. *J. Atmos. Ocean. Technol.* **2001**, *18*, 830–850. [[CrossRef](#)]
56. Guerova, G.; Jones, J.; Douša, J.; Dick, G.; de Haan, S.; Pottiaux, E.; Bock, O.; Pacione, R.; Elgered, G.; Vedel, H.; et al. Review of the state of the art and future prospects of the ground-based GNSS meteorology in Europe. *Atmos. Meas. Technol.* **2016**, *9*, 5385–5406. [[CrossRef](#)]
57. Wibig, J.; Siedlecki, M. Przestrzenny i czasowy rozkład zawartości wody opadowej w atmosferze nad Europą (1958–2005). In *Wahania Klimatu w Różnych Skalach Przestrzennych i Czasowych*; Piotrowicz, K., Twardosz, R., Eds.; Instytut Geografii i Gospodarki Przestrzennej, Uniwersytet Jagielloński: Kraków, Poland, 2007; pp. 195–204. (In Polish)
58. Cossu, F.; Hocke, K. Influence of microphysical schemes on atmospheric water in the Weather Research and Forecasting model. *Geosci. Model Dev.* **2014**, *7*, 147–160. [[CrossRef](#)]
59. Kożuchowski, K.M. Zawartość wody opadowej w atmosferze i opady w Polsce. *Przeg. Geofiz.* **2016**, *LXI(3–4)*, 151–169. (In Polish).
60. Degirmendžić, J.; Kożuchowski, K. Mediterranean cyclones, the atmospheric moisture content and precipitation in Poland. *Geogr. Pol.* **2017**, *90*, 5–20. [[CrossRef](#)]
61. Araszkiwicz, A.; Kiliszek, D.; Mierzwiak, M.; Nowak Da Costa, J.; Szolucha, M. GPS –Based Multi-Temporal Variation in Precipitable Water over Territory of Poland. *Remote Sens.* **2021**, *13*, 2960. [[CrossRef](#)]
62. Skamarock, W.C.; Klemp, J.B.; Dudhia, J.; Gill, D.O.; Barker, D.M.; Duda, M.; Huang, X.Y.; Wang, W.; Powers, J.G. *A Description of the Advanced Research WRF Version 3*; Technical report TN-475+STR: June 2008; NCAR: Boulder, CO, USA, 2008.
63. Dee, D.P.; Uppala, S.M.; Simmons, A.J.; Berrisford, P.; Poli, P.; Kobayashi, S.; Andrae, U.; Balsameda, M.A.; Balsamo, G.; Bauer, P.; et al. The Era-Interim reanalysis, configuration and performance of the data assimilation system. *Q. J. R. Meteorol. Soc.* **2011**, *137*, 553–597. [[CrossRef](#)]
64. Kryza, M.; Werner, M.; Wałaszek, K.; Dore, A.J. Application and evaluation of the WRF model for high-resolution forecasting of rainfall—A case study of SW Poland. *Meteorol. Z.* **2013**, *22*, 595–601. [[CrossRef](#)]
65. Kryza, M.; Wałaszek, K.; Ojrzyńska, H.; Szymanowski, M.; Werner, M.; Dore, A.J. High resolution dynamical downscaling of ERA-Interim using the WRF regional climate model for the area of Poland. Part 1, model configuration and statistical evaluation for the 1981–2010 period. *Pure Appl. Geophys.* **2017**, *174*, 511–526. [[CrossRef](#)]
66. Wałaszek, K.; Kryza, M.; Werner, M. Evaluation of the WRF meteorological model results during a high ozone episode in SW Poland—The role of model initial conditions. *Int. J. Environ. Pollut.* **2014**, *54*, 193–202. [[CrossRef](#)]
67. Iacono, M.J.; Delamere, J.S.; Mlawer, E.J.; Shephard, M.W.; Clough, S.A.; Collins, W.D. Radiative forcing by long-lived greenhouse gases, Calculations with the AER radiative transfer models. *J. Geophys. Res.-Atmos.* **2008**, *113*, D13103. [[CrossRef](#)]
68. Mlawer, E.J.; Taubman, S.J.; Brown, P.D.; Iacono, M.J.; Clough, S.A. Radiative transfer for inhomogeneous atmospheres: RRTM, a validated correlated-k model for the longwave. *J. Geophys. Res.-Atmos.* **1997**, *102*, 16663–16682. [[CrossRef](#)]
69. Hong, S.-Y.; Noh, Y.; Dudhia, J. A New Vertical Diffusion Package with an Explicit Treatment of Entrainment Processes. *Mon. Weather Rev.* **2006**, *134*, 2318–2341. [[CrossRef](#)]
70. Kain, J.S. The Kain–Fritsch Convective Parameterization, an update. *J. Appl. Meteorol.* **2004**, *43*, 170–181. [[CrossRef](#)]
71. Tao, W.-K.; Simpson, J.; McCumber, M. An Ice-Water Saturation Adjustment. *Mon. Weather Rev.* **1989**, *117*, 231–235. [[CrossRef](#)]
72. *Vaisala, Comparison of Vaisala Radiosondes RS41 and RS92*; White Paper; Ref. B211317EN-B © Vaisala: Helsinki, Finland, 2014.
73. Miloshevich, L.M.; Vömel, H.; Whiteman, D.N.; Leblanc, T. Accuracy assessment and correction of Vaisala RS92 radiosonde water vapor measurements. *J. Geophys. Res.* **2009**, *114*, D11305. [[CrossRef](#)]
74. *NCAR Command Language Software, Version 6.6.2*; UCAR/NCAR/CISL/TDD: Boulder, CO, USA, 2019. [[CrossRef](#)]
75. R Core Team. *A Language and Environment for Statistical Computing*; R Foundation for Statistical Computing: Vienna, Austria; ISBN 3-900051-07-0. Available online: [R-project.org](https://www.R-project.org) (accessed on 14 June 2013).
76. Trenberth, K.; Fasullo, J.; Smith, L. Trends and variability in column-integrated atmospheric water vapor. *Clim. Dyn.* **2005**, *24*, 741–758. [[CrossRef](#)]
77. Chen, B.Y.; Liu, Z.Z. Global water vapor variability and trend from the latest 36 year (1979 to 2014) data of ECMWF and NCEP reanalyses, radiosonde, GPS, and microwave satellite. *J. Geophys. Res. Atmos.* **2016**, *121*, 11442–11462. [[CrossRef](#)]
78. Nayak, S.; Takemi, T. Dependence of extreme precipitable water events on temperature. *Atmosfera* **2019**, *32*, 159–165. [[CrossRef](#)]
79. Zveryaev, I.I.; Wibig, J.; Allan, R.P. Contrasting interannual variability of atmospheric moisture over Europe during cold and warm seasons. *Tellus A* **2008**, *60*, 32–41. [[CrossRef](#)]
80. Wang, Y.; Zhang, Y.; Fu, Y.F.; Li, R.; Yang, Y.J. A climatological comparison of column-integrated water vapor for the third-generation reanalysis datasets. *Sci. China Earth Sci.* **2016**, *59*, 296–306. [[CrossRef](#)]
81. Jiang, J.; Zhou, T.J.; Zhang, W.X. Evaluation of Satellite and Reanalysis Precipitable Water Vapor Data Sets Against Radiosonde Observations in Central Asia. *Earth Space Sci.* **2019**, *6*, 1129–1148. [[CrossRef](#)]
82. Varga, A.J.; Breuer, H. Evaluation of convective parameters derived from pressure level and native ERA5 data and different resolution WRF climate simulations over Central Europe. *Clim. Dyn.* **2022**, *58*, 1569–1585. [[CrossRef](#)]
83. Taszarek, M.; Pilguy, N.; Allen, J.T.; Gensini, V.; Brooks, H.E.; Szuster, P. Comparison of Convective Parameters Derived from ERA5 and MERRA-2 with Rawinsonde Data over Europe and North America. *J. Clim.* **2021**, *34*, 3211–3237. [[CrossRef](#)]
84. González, A.; Expósito, F.J.; Pérez, J.C.; Díaz, J.P.; Taima, D. Verification of precipitable water vapour in high-resolution WRF simulations over a mountainous archipelago. *Q. J. R. Meteorol. Soc.* **2013**, *139*, 2119–2133. [[CrossRef](#)]

85. Fedele, F.; Miglietta, M.M.; Perrone, M.R.; Brizzzi, P.; Bellotti, R.; Conte, D.; Guarnieri Calò Carducci, A. Numerical simulations with the WRF model of water vapour vertical profiles, a comparison with LIDAR and radiosounding measurements. *Atmos. Res.* **2015**, *166*, 110–119. [[CrossRef](#)]
86. Diaz, L.R.; Santos, D.C.; Kafer, P.S.; Iglesias, M.L.; da Rocha, N.S.; da Costa, S.T.L.; Kaiser, E.A.; Rolim, S.B.A. Reanalysis profile downscaling with WRF model and sensitivity to PBL parameterization schemes over a subtropical station. *J. Atmos. Sol. Terr. Phys.* **2021**, *222*, 105724. [[CrossRef](#)]
87. Johnsen, K.P.; Rockel, B. Validation of a regional weather forecast model with GPS data. *Phys. Chem. Earth.* **2001**, *26*, 415–419. [[CrossRef](#)]
88. Westwater, E.R.; Crewell, S.; Matzler, C. Surface-based microwave and millimeter wave radiometric remote sensing of the troposphere, a tutorial. *IEEE Geosci. Remote Sens. Soc. Newsl.* **2005**, *134*, 16–33.
89. McGrath, R.; Semmler, T.; Sweeney, C.; Wang, S. Impact of balloon drift errors in radiosonde data on climate statistics. *J. Clim.* **2006**, *19*, 3430–3442. [[CrossRef](#)]
90. Morland, J.; Mätzler, C. Spatial interpolation of GPS integrated water vapour measurements made in the Swiss Alps. *Meteorol. Appl.* **2007**, *14*, 15–26. [[CrossRef](#)]
91. Cossu, F.; Hocke, K.; Martynov, A.; Martius, O.; Mätzler, C. Atmospheric water parameters measured by a ground-based microwave radiometer and compared with the WRF model. *Atmos. Sci. Lett.* **2015**, *16*, 465–472. [[CrossRef](#)]
92. Schrader, F.; Durner, W.; Fank, J.; Gebler, S.; Putz, T.; Hannes, M.; Wollshlager, U. Estimating precipitation and actual evapotranspiration from precision Lysimeter measurements. *Procedia Environ. Sci.* **2013**, *19*, 543–552. [[CrossRef](#)]
93. Ross, R.J.; Elliot, W.P. Radiosonde-based Northern Hemisphere tropospheric water vapor trends. *J. Clim.* **2001**, *14*, 1602–1612. [[CrossRef](#)]
94. Zhang, Y.H.; Xu, J.W.; Yang, N.; Lan, P. Variability and Trends in Global Precipitable Water Vapor Retrieved from COSMIC Radio Occultation and Radiosonde Observations. *Atmosphere* **2018**, *9*, 174. [[CrossRef](#)]